Available online at www.sciencedirect.com

ScienceDirect

MATTER AND RADIATION AT EXTREMES

Matter and Radiation at Extremes 2 (2017) 149−176

www.journals.elsevier.com/matter-and-radiation-at-extremes

Review Article

P3: An installation for high-energy density plasma physics and ultra-high intensity laser−matter interaction at ELI-Beamlines

S. Weber*, S. Bechet, S. Borneis, L. Brabec, M. Bučka, E. Chacon-Golcher, M. Ciappina, M. DeMarco, A. Fajstavr, K. Falk, E.-R. Garcia, J. Grosz, Y.-J. Gu, J.-C. Hernandez, M. Holec, P. Janečka, M. Jantač, M. Jirka, H. Kadlecova, D. Khikhlukha, O. Klimo, G. Korn, D. Kramer, D. Kumar, T. Lastovička, P. Lutoslawski, L. Morejon, V. Olšovcová, M. Rajdl, O. Renner, B. Rus, S. Singh, M. Šmid, M. Sokol, R. Versaci, R. Vrána, M. Vranic, J. Vyskočil, A. Wolf, Q. Yu

ELI-Beamlines, Institute of Physics, Academy of Sciences of the Czech Republic, 18221 Prague, Czech Republic

Received 30 January 2017; revised 6 March 2017; accepted 24 March 2017
Available online 14 April 2017

Abstract

ELI-Beamlines (ELI-BL), one of the three pillars of the Extreme Light Infrastructure endeavour, will be in a unique position to perform research in high-energy-density-physics (HEDP), plasma physics and ultra-high intensity (UHI) ($>10^{22}\mathrm{W/cm^2}$) laser−plasma interaction. Recently the need for HED laboratory physics was identified and the P3 (plasma physics platform) installation under construction in ELI-BL will be an answer. The ELI-BL 10 PW laser makes possible fundamental research topics from high-field physics to new extreme states of matter such as radiation-dominated ones, high-pressure quantum ones, warm dense matter (WDM) and ultra-relativistic plasmas. HEDP is of fundamental importance for research in the field of laboratory astrophysics and inertial confinement fusion (ICF). Reaching such extreme states of matter now and in the future will depend on the use of plasma optics for amplifying and focusing laser pulses. This article will present the relevant technological infrastructure being built in ELI-BL for HEDP and UHI, and gives a brief overview of some research under way in the field of UHI, laboratory astrophysics, ICF, WDM, and plasma optics.

PACS Codes: 52.25.Fi; 52.27.Ep; 52.27.Ny; 52.35.Mw; 52.38.Fz; 52.38.Dx; 52.38.Kd; 52.38.Mf; 52.57.-z; 52.65.-y; 52.72.+v

Keywords: High-energy-density-physics; Ultra-high-intensity; Warm dense matter; Laboratory astrophysics; High repetition rate lasers; Plasma optics; Inertial confinement fusion; Laser−plasma interaction; Relativistic plasmas

1. Introduction

Ever since the invention of the laser there has been a constant push for ever higher power-levels and correspondingly higher intensities of the focused pulse. Since the invention of chirped-pulse-amplification (CPA), the power available has increased many orders of magnitude [1−3]. In parallel the scientific demand for multiple, synchronized laser beam in the same interaction chamber has increased in order to be able to perform sophisticated pump-probe experiments. In this context ELI (Extreme Light Infrastructure) is the latest large-scale effort in Europe to push for new, state-of-the-art, high repetition rate laser systems. ELI is part of the European ESFRI (European Strategy Forum on Research Infrastructures) roadmap. ELI is expected to be the first worldwide laser facility to provide an unprecedented power-level of 10 Petawatt. These new laser

* Corresponding author.
E-mail address: stefan.weber@eli-beams.eu (S. Weber).
Peer review under responsibility of Science and Technology Information Center, China Academy of Engineering Physics.

http://dx.doi.org/10.1016/j.mre.2017.03.003

systems will consequently allow to perform research in physics areas which were hitherto impossible.

This article provides a description of one of the experimental halls, E3, of the ELI-Beamlines user facility, which houses the *Plasma Physics Platform* (P3). It gives an overview of the technological infrastructure and explains the capabilities for the future user community. It also gives a brief overview of some of the physics research that will be performed there.

The remainder of the article is organized as follows. Sec. 2 gives an overview of the Extreme Light Infrastructure Beamlines. Sec. 3 summarizes briefly the kind of physics the installation is expected to investigate. The building structure and radiation/activation issues are briefly presented in Secs. 4 and 5, respectively. In the following section, Sec. 6, the vacuum and beam transport system is described. The main experimental infrastructure is presented in Sec. 7 and the laser configuration in Sec. 8. Sec. 9 gives some examples of the kind of research which is expected to be pursued in P3 and Sec. 10 discusses some aspects of high-field interaction. Some of the technology development efforts are presented in Sec. 11. In Sec. 12 the importance of local high-performance computing and simulation support is pointed out. Finally, in Sec. 13 a conclusion and an outlook are presented.

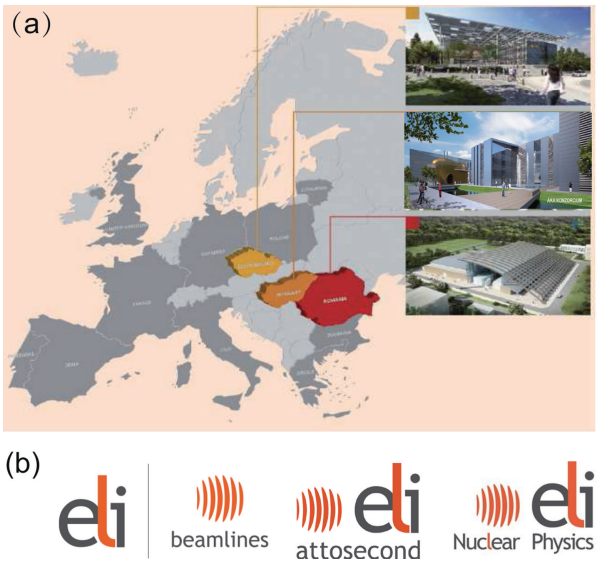

Fig. 1. (a) The three pillars of ELI are located in Czech Republic, Hungary and Romania [4]. ELI-Beamlines (Czech Republic) provides dedicated sources of particles and radiation, ELI-Atto (Hungary) concentrates on atto-second related physics and sources, and ELI-NP (Romania) will perform nuclear physics research with lasers. (b) The logos of the three pillars.

2. ELI and ELI-Beamlines

ELI [4–6] is intended as an open user facility for laser-based research. It will be at the disposition of the academic community as much as the industrial sector. It will provide research tools based on new high repetion-rate and high-power laser systems. ELI is a major endeavour of the European Union to advance laser-based research and drive development of new laser technology. ELI is composed of three pillars with different specialization (see Fig. 1) located in Czech Republic (Dolni Brezany near Prague), Hungary (Zeged) and Romania (Margurele near Bukarest). The present article presents one of the experimental halls and its technology and research programs of ELI-Beamlines [7]. The *Extreme* Light Infrastructure [4,8] can be considered at the same time to be an *European* Light Infrastructure.

3. The physics setting

The P3 installation was from the beginning designed to be a multi-purpose, versatile research platform for laser–plasma interaction in the widest sense. Contrary to other installations of ELI-BL it is not supposed to provide well-characterized, reliable secondary sources of particles and radiation. It is expected to be an installation where fundamental research is conducted in the fields of ultra-high intensity laser–matter interaction and high-energy-density physics in the broadest sense. In particular research related to the following topics are perfectly suited for this installation:

- *Laboratory Astrophysics* (collisionless shocks, cosmic ray physics, magnetic reconnection, jet formation, radiation hydrodynamics etc.) [9–13].
- *Ultra-High Intensity* (radiation damping, electron–positron pair generation, vacuum birefringence, γ-ray flashes, relativistic flying mirror etc.) [14–18].
- *Warm Dense Matter and High-Energy Density Physics* (planetary cores, shock waves, thermonuclear fusion for energy, opacities, equation of state, phase transition of new states of matter etc.) [19–21].
- *Laser-Plasma Interaction* (e.g. for the shock-ignition scheme of ICF, parametric instabilities, soliton formation, laser absorption etc.) [22–24].
- *Plasma Optics* (plasma amplification, plasma focusing, new schemes for future high-power laser pulses, manipulation of coherent light by plasmas etc.) [25–27].

Many of these topics of course overlap and are strongly interdependent. Although initially oriented towards fundamental resarch, P3 will engage in the development of new secondary sources which are then optimized and applied by other groups. The longterm perspective for future societal applications is therefore assured. This very large area of research possibilities is due to the availability of laser beams which cover a temporal range from femtoseconds to nanoseconds and an energy range from tens of Joules to kilo-Joule (see Sec. 8). This becomes possible due to the uniqueness of the 10 PW laser at ELI-BL (L4, see Sec. 8) which has a long pulse length of 150 fs. This implies 1.5 kJ of energy. This amount of energy allows at the same time to perform fundamental experiments related to warm dense matter (e.g. driving strong shocks), laboratory astrophysics (e.g. generating magnetic fields) and laser–plasma interaction for inertial confinement fusion (e.g. parametric instabilities and transport). ELI-BL will therefore be in the position to perform new research in the short-pulse as well as long-pulse regime.

4. The building infrastructure and layout

Fig. 2 shows the actual building of ELI-Beamlines. It is a multi-functional complex comprising office space, laboratories, workshops, public areas and the three-storage laser and experiment building. Nearby are additional buildings for storage and large-scale workshops.

The concrete structure hosting the experimental halls and the laser bays is shown in Fig. 3.

Fig. 2. Architecture snapshots of the ELI-Beamlines building as of 2016.

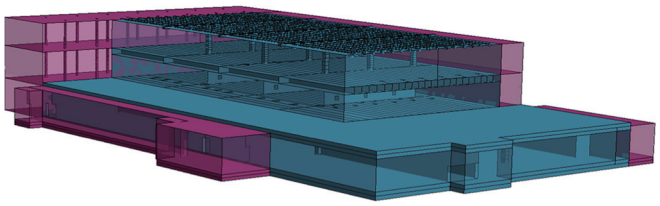

Fig. 3. The experimental building of ELI-BL. The part in blue color is a single monolithic concrete block providing perfect stability and vibration properties. The parts shown in pink color are decoupled from the experimental halls and laser halls (shown in blue) and contain support infrastructure such as roughing pumps. The overall dimensions are roughly 100 m × 50 m for the lowest floor level.

The lowest floor of the experimental building hosts the experimental halls (E1-E6) and the hall L4c for the 10 PW compressor as shown in Fig. 4. Each hall is dedicated to specific research areas such as imaging and bio-medical applications (E1), X-ray generation (E2), plasma physics and high-field science (E3), ion acceleration (E4) and electron acceleration and undulator setup (E5). The second floor contains the four laser halls (L1–L4) for the four laser systems available in ELI-BL. The top floor provides support infrastructure for the lasers such as cooling, capacitor banks etc.

To establish a baseline design of the beam transport super structures and mounts the vibrations of the building floor, the wall and the ceiling were measured. Due to the fact that most infrastructures is not yet running, the stiffness of the building was measured to generate a dynamic impact FEA (finite element analysis) model for different static and dynamic loads that are considered to be representative for the future vibration levels during the operation phase of the facility. The measured stiffness and ambient vibrations were the basis for the dynamic impact optimized tower, mirror breadboard design and also for the entire vacuum system including its pipe supports. The laser and experimental building exhibits a unique stability, acting basically as a gigantic optical table (see Fig. 5). This stems from the fact that the complex is sitting on a gigantic rock and being itself extremely massive. The laser and experimental building contains about 35,000 m^3 of concrete and 10,000 tons of steel (the weight of the Eiffel tower in Paris). This kind of stability is essential for transporting the laser beams over very long paths from the compressor to the various experimental halls.

The total power consumption of the ELI-BL facility is initially expected to be of the order of $\sim$ 2.5 MW comprising laser and experimental building, laboratories and office complex.

5. Radiation and activation issues

Radiation and nuclear activation are an intrinsic part of high-power laser facilities [28].

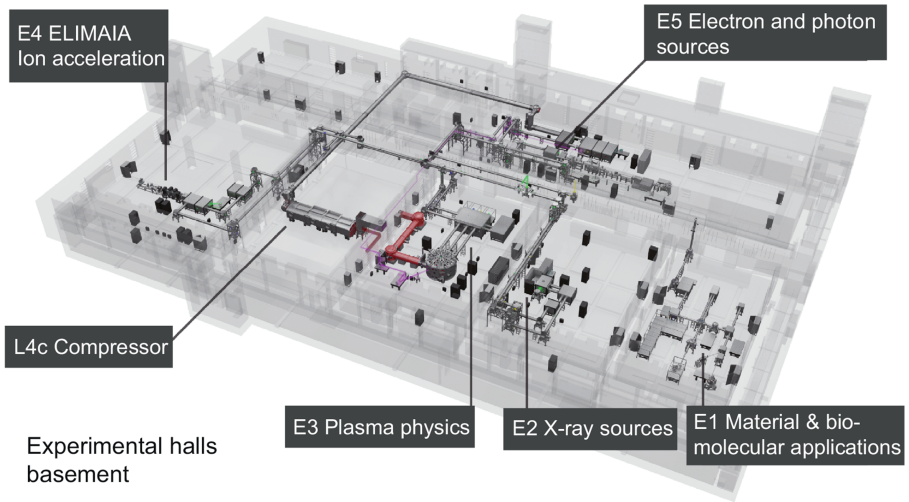

Fig. 4. The ground floor of the experimental and laser building, displaying the six experimental halls and the hall containing the 10 PW compressor (L4c). The plasma physics platform (P3) is located in the experimental hall E3, adjacent to the compressor hall L4c.

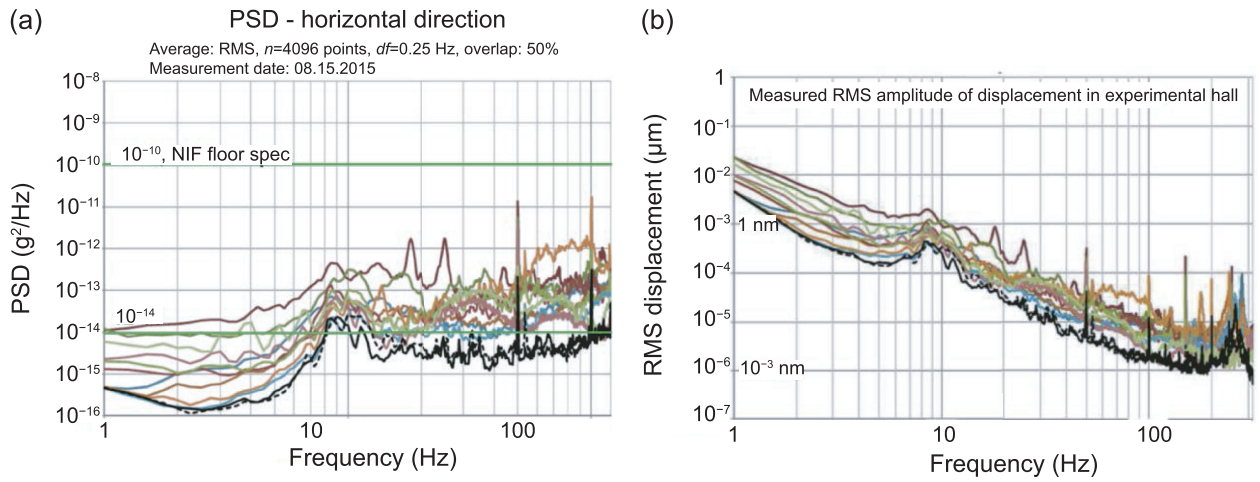

Fig. 5. (a) Random vibration power spectral density (PSD) for vibrations in the horizontal direction. Shown also the floor specifications for NIF (National Ignition Facility of LLNL in the USA). (b) RMS displacement for random vibration, showing oscillation amplitudes of 1 nm ($= 0.001\mu$m) and below in the relevant frequency. The mean square response or displacement of a SDOF (Single-degree-of-freedom) oscillating system is proportional to $\sim \mathrm{PSD}/\omega_0^3$, where ω_0 is the natural frequency or Eigenfrequency. Any design of optical elements therefore needs to push up the Eigenfrequency of the device as much as possible.

The operation of P3 will result in the production of high energy mixed radiation fields. Administrative, passive (shielding), and active (area and personnel monitoring, interlocks) measures are being implemented to ensure safe and efficient operation of P3, the E3 experimental hall and adjacent areas. The radiation protection assessments are based on Monte Carlo simulations, using FLUKA [29–31]. All the simulations are being performed for the worst-case scenario in terms of radiation protection, i.e. the one which generates the highest levels of ionizing radiation. Both prompt and residual radiation need to be considered.

Initially, in the design phase of the main civil structure, the knowledge of the experimental setup and source term were very limited and therefore the simulations were accordingly very simplified. These simulations served as a basis for bulk shielding design (walls, main penetrations). As of now, as the start of P3 operation is approaching, the level of simulation detail increases. The experimental chamber and the building have been carefully modeled in terms of both geometry and materials. The worst-case scenario, which is being considered, is the interaction of the 10 PW laser with a solid target.

The source term for the simulations has been obtained by PIC simulations. The radiation generated in the laser–target interaction will have large opening angles and will be made up mostly of photons ($> 10^{14}$ γ/shot, $E \simeq 16$ MeV) and protons (3×10^{11} p/shot, energy spectrum peaked at low energies with a long tail up to 1 GeV).

The ambient dose equivalent rate maps obtained are shown in Fig. 6. Due to the high radiation levels, the presence of personnel inside the experimental hall, is forbidden during the laser operation. As full P3 operation may impose some access restrictions on the adjacent halls, implementation of mitigation measures is foreseen.

For activation studies, three irradiation profiles (1 year, 1 month, 1 day) with up to 120 shots/day have been considered. Activation studies were performed to assess the amount of radioactive waste generated, and the possible limitation of time spent in the hot spots vicinity.

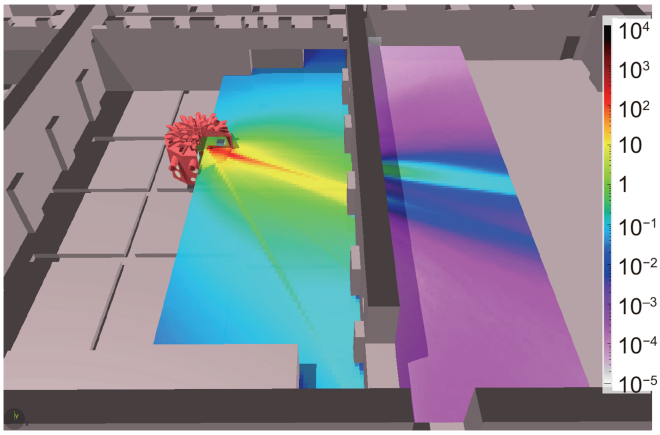

Fig. 6. Ambient dose equivalent rate map in mSv/shot for the experimental hall E3 originating from experiments performed in P3. All doors are assumed open.

The calculated induced activation of the chamber and its content are shown in Fig. 7. In the most likely experimental scenario, access to the chamber will be desired every day during a campaign. For a shot sequence of 120 shots which corresponds to an optimistic scenario of 1 day of experiments, the chamber is expected to have an ambience dose equivalent activity (shown on the axis on the left) of 0.7 μSv/h after a cool down time of about 40 min. If a person were to access the chamber at this ambient activity, then he/she will be able to spend about 600 h inside the chamber per year (shown on the axis on the right) to stay within the limit of annual exposure of less than 1 mSv.

Further, activation of the concrete was assessed and the results compared with the specific activity legal limit for radioactive waste [32,33]. Simulations indicate that the specific activity of $^{56}_{25}$Mn and $^{132}_{55}$Cs will be above the threshold. Nevertheless, because of the short lifetimes, less than two weeks would be needed to return below the legal limit.

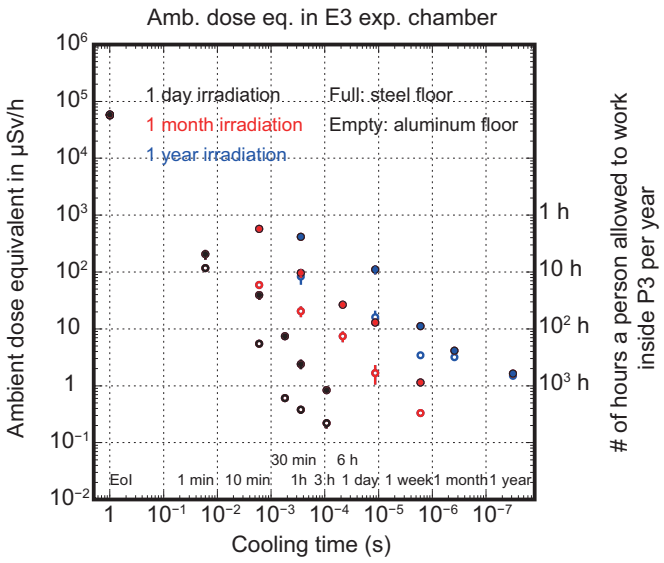

Fig. 7. Maximum of ambient dose equivalent inside the E3 experimental chamber P3 as a function of time, for different irradiation profiles. The steel data is for reference purpose as the chamber is made of Aluminum entirely. The scale on the right also corresponds to the number of hours a person is allowed to work inside P3 per year.

Naturally, more simulations will be performed to asses all the E3 configurations. However, the results indicate that, even in the most challenging set up, the activation of materials should not limit the use of experimental hall, while simple mitigation actions could be implemented to take care of the prompt radiation.

6. The beam transport system

The complex high-intensity beam transport system of the compressed 30 fs, 10 Hz L3 beam over up to 88 m and up to 18 mirror reflections presents a major engineering effort. This system will be the world's first and longest distance high average power PW beam transport system ever built posing serious challenges onto the vibration stability of the laser building, the mirror towers, the opto-mechanics as well as on the performance of the high-power and highest damage threshold mirrors.

The top-level requirements for the beam transport system are summarized in Fig. 8.

Vacuum level	10^{-5} mbar
Cleanliness required	Particle level ~100 (TBD) and NVR level ~A/10 = 0.1 μg/cm^2 per MIL-STD-1246C
Pointing stability error budget for entire L3 BT	Max 1 μrad
Pointing stability per BT turn point	Max 100 nrad mechanical, 200 nrad optical
Alignment system	Concept for far and near field measurement easy automation
Initial installation alignment, placing of all components	Installation and pre-alignment with laser tracker
Wavefront Correction	52 actuator full size deformable mirror with closed loop wavefront sensing

Fig. 8. List of top-level requirements for the L3 beam transport sytem.

Fig. 9 gives a schematic overview of the L3 (see Sec. 8) beam transport system with its various components.

The L3 beam transport system will be equipped with an alignment laser (AL) that may be injected instead of the L3 laser beam into the Upper Injection Chamber (UI) and subsequently collinearly propagated to the L3 beam axis and focused with the target parabolas. The alignment laser will allow the commissioning of the planned adaptive optics loops and to assess the focus quality and the pointing stability of the beam transport system. The lower Injection Chamber (IC) is the entrance to the beam transport system. It will contain a 180° Rotation Unit (RU) to either guide the beam to E3, E4 and E5 or, when 180° rotated, to E2 (see Fig. 10). To reflect the beam to E3 a Switchyard Chamber (SWC) is equipped with a Translation Stage (TS) that moves an insertable turn mirror from the outside position into the beam. In outside position the L3 laser propagates straight to E4. The same type switchyard chamber will allow dispatching the beam to E5.

The conceptual design overview of the L3 beam transport system in its initial phase is shown in Fig. 10. In Fig. 11 the

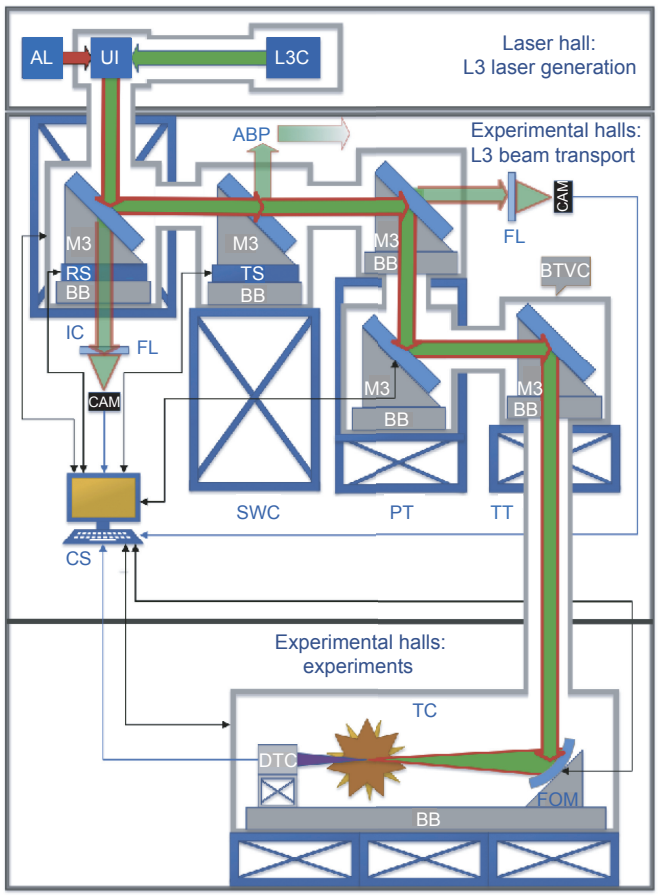

Fig. 9. Schematics of the L3 beam transport system. Legend: ABP: Alternative/another beam-path from switchyard, AL: Alignment laser, BB: Breadboard, BTVC: Beam transport vacuum enclosure (vacuum vessels and pipes), CAM: Camera, CS: Control system, DTC: Detector, FL: Lens, FOM: Focusing optics and its mount, IC: Injection chamber, L3C: L3 Compressor, M3: Motorized mirror mount, PT: Periscope tower, RS: Rotational stage, SWC: Switchyard chamber/tower, TS: Translation stage, TT: Turning tower/chamber/mirror, TC: Target chamber, UI: Upper injector chamber.

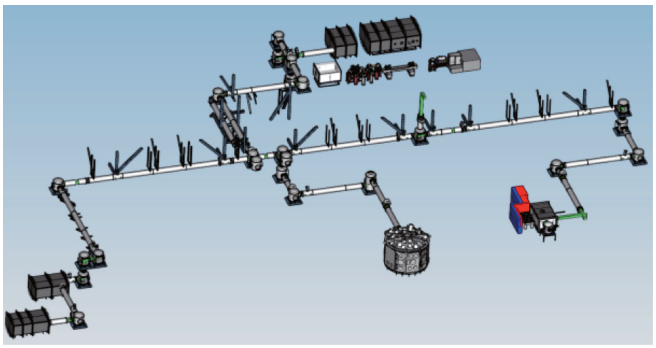

Fig. 10. Conceptual design of the L3 beam transport system to various experimental halls. The shown beam distribution system is located in the basement of the 110 m long laser building. The injection point of the L3 laser is one floor above where the laser system itself and the compressor are located.

Fig. 11. The initial bypass of the L3 beam transport in the experimental hall E3.

initiall bypass construction for E3 is shown which will be used till the optical switchyard becomes available. The beam transport system for the L3 laser will be constructed of DN500 pipes made of stainless steel, except in the vicinity of the P3 chamber where transport will switch over to aluminum due to activation issues (see Sec. 5).

To limit the target displacement of the beam to a maximum of 2 μm, each single beam guiding component must have displacements of the order of $d < 0.1$ μm and rotations of the order of $\phi < 0.01$ μrad. The overall beam target displacement (btd) is given by the formula:

$$\mathrm{btd} = \sqrt{\sum_{i=1}^{n} [L_i \tan(\varphi_i) + d_i]^2}. \quad (1)$$

Here, L_i is the distance of the laser component to the target, φ_i the vibration rotation angle of the component, d_i the vibration displacement of the component, and n_i the identification number of the component (mirror, grating, parabola etc.).

Fig. 12 presents an analysis of the gravity sag acting on the beam transport periscope mirrors as a function of the substrate thickness and the number and location of the mirror mount support points. The gravity sag induces a deformation of the wave front and needs to minimized as much a possible. At a substrate thickness of 75 mm the reflected wavefront deformation caused by the gravity sag is only 55 nm and thus negligible.

Fig. 13 shows the conceptual design of the beam transport for the large-aperture L4f 10 PW beam, which is transported through the wall from the adjacent L4 compressor in hall L4c directly into the interaction chamber. The diameter of beam tubes will be DN1000. As for the L3 transport, pipes will be made of aluminum in the vicinity of the P3 chamber. Note that the total vacuum energy stored in the beam transport system is of the order of 6 Mega Joules. For the complete vacuum system including all experimental chambers and compressors the stored energy will amount to ∼ 30 MJ. Engineering rules known from large particle accelerators will be applied for safe operation.

The turn mirror requirements (see Fig. 14) are set by the L3 laser parameters that need to be preserved during 88 m of propagation and with up to 18 mirror reflections. This challenge of guiding the L3 laser precisely onto target is by far non-trivial. The measured LDT (laser damage threshold) of first coating witness samples is 800 $\mathrm{mJ/cm^2}$ measured with the Atlas laser in Munich and was also measured at the PALS laser facility. The maximum fluence of the ideal L3 laser pulses is 70 $\mathrm{mJ/cm^2}$. Thus the L3 beam transports system will have 10 times of margin for amplitude modulations occurring during free propagation of up to 88 m. This is the justification to build the system at least initially for commissioning and first experiments without a very complex reflective relay imaging system.

7. The plasma physics platform (P3) and associated infrastructure

Fig. 15 shows the overall layout of the experimental hall E3. The main elements are the central vacuum chamber (P3), the optical switchyard (MOB) and the beam transport system (as presented in the previous Sec. 6).

The main interaction chamber, P3, is shown in Fig. 16. P3 has a decagonal body of ∼ 4.5 m inner diameter and ∼ 3.4 m height. The volume is roughly 50 $\mathrm{m^3}$. It is fabricated entirely of Aluminum due to activation issues (see Sec. 5). The total weight is of the order of ∼ 14 tons.

Plasma physics experiments will require frequent vacuum breaking. To minimize turnover time very strong vacuum pumps will be set up to assure pump-down times to 10^{-6}mbar of the order of 15 min. The characteristics of the pumps are:

- roughing pump capacity: 5000 $\mathrm{m^3/h}$,
- cryo pumps: 2×10^4 liter/s,
- turbo-molecular pumps: 2×3200 liter/s.

The small diameter beams (L2, L3, L4p) are brought in from the top of the chamber and then deflected downwards, whereas the large diameter beam L4f comes in mid-level and determines TCC. The uncompressed beam L4n can be brought in mid-level from any side as it is transported under air. Fig. 17 shows the layout of the 10 PW inside P3. A modular

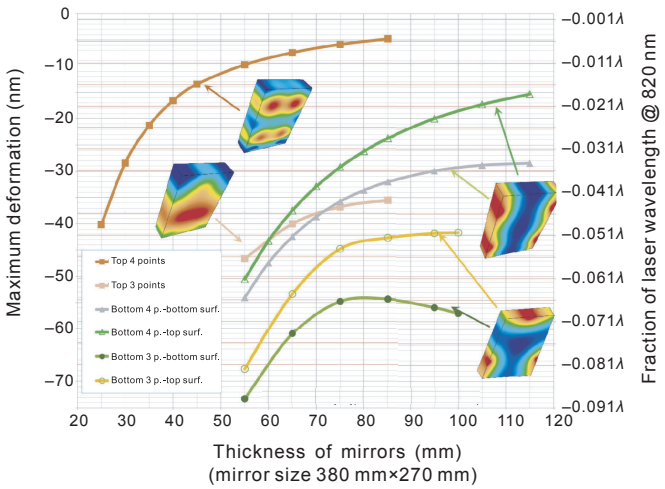

Fig. 12. Finite element analysis of mirror deformations due to gravity sag. The maximum deformation is given in nanometers (left scale) and fraction of the laser wavelength (right scale, for a nominal center wavelength of the laser of 820 nm) as function of the slab thickness in millimeters for various support configurations of the mirror. Inset explanation: top, bottom, and vertical refers to the mirror orientation (upper, lower periscope mirror and standing). The legend (6 points, 4p. etc.) refer to the number of support points of the slab by the mirror mount. The unrealistic thick samples show the inadequateness of the three-point support mounts.

breadboard structure allows for large flexibility in experimental setups. The parabola mount for the large-size 10 PW beam will be sitting directly on the baseplate of the chamber.

P3 has no principal restrictions on the kind of targetry to be used. Gaseous, liquid, solid, foam or frozen materials will be employed as target material. In particular newly developed targetry such as extremely high density gas jets (above critical density n_c [34]) and hydrogen ice [35] will be used.

The MOB (Magic Optical Box) functions as an optical switchyard relaying the laser beams L3 and L4p (and in future can also accomodate L2) to P3. It contains the delay lines and allows for additional manipulations of the laser beams (frequency conversion, beam splitting, deriving pick-off beam, splitting of beams, deformable mirrors, polarizers, pockel cells etc.).

An additional piece of technology is the long focal length set-up which is a small movable vacuum chamber with a spherical mirror to allow for focal lengths up to 5 m. It also is the essential ingredient for the betatron (see Sec. 11.3).

8. Laser configuration

The overall laser configuration of ELI-BL is displayed in Fig. 18. The laser L1 is not of interest to P3 research. Initially the two important laser systems for P3-research will be L3 and L4.

The basic characteristics of the laser beams of ELI-BL and those available in P3 are summarized in Table 1. L2, L3, L4p and L4f are transported under vacuum and L4n, at least initially, under air. P3 will have access to fully synchronized simultaneous operation of up to 5 laser beams for sophisticated pum-probe experiments.

The laser beams L4n, L4p and L4f are derived from the original L4 laser beam by a double splitting procedure as shown in Fig. 19. Most likely specific machine states will

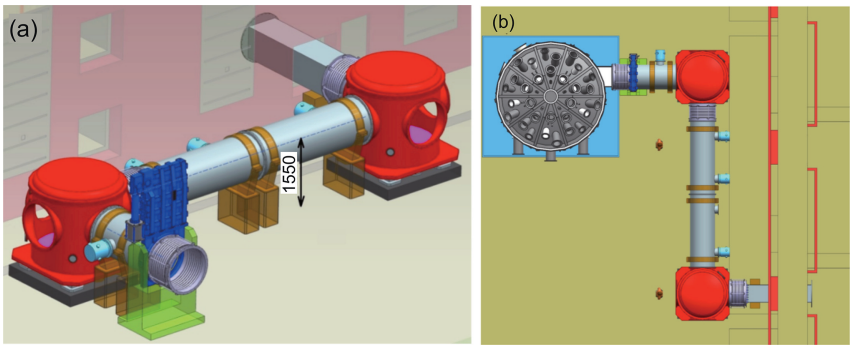

Fig. 13. Conceptual design of the L4 beam transport. (a) Isometric view of the long solution. (b) Corresponding top view.

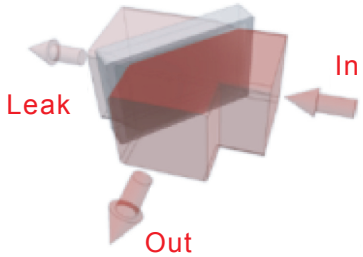

Dimensions	440 mm× 290 mm× 75 mm
Damage threshold @30 fs in vacuum	0.7 J/cm^2 1000-on-1 @>10 Hz, @30 fs
Center wavelength	820 nm
Bandwidth	770-870 nm
Reflectivity R_s	>99.8%
Reflectivity R_p	>99.5%
GDD	<40 fs^2
Front surface S1 single pass reflected wavefront at use angle over 90% of CA	<95 nm (0.15 waves at 633 nm) *P-V*

Fig. 14. The most important specifications of the L3 mirrors.

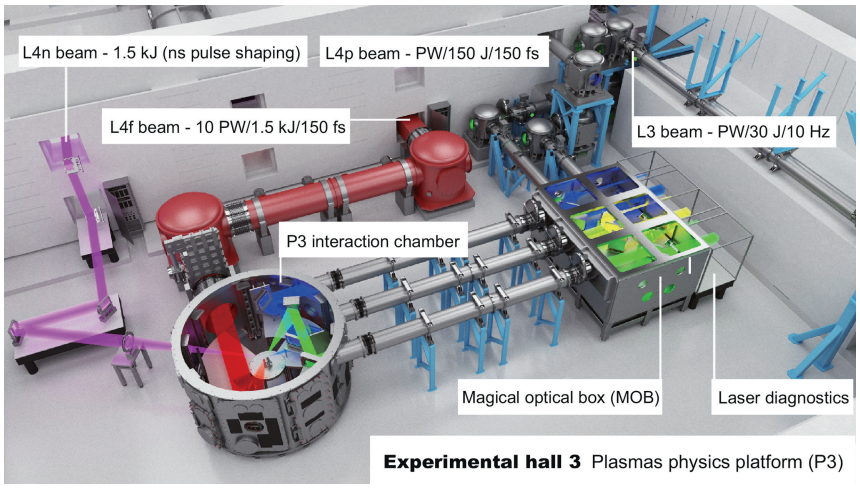

Fig. 15. Design picture of the expected final layout of the experimental hall E3. The details of the beam transport will probably change due to constructional constraints.

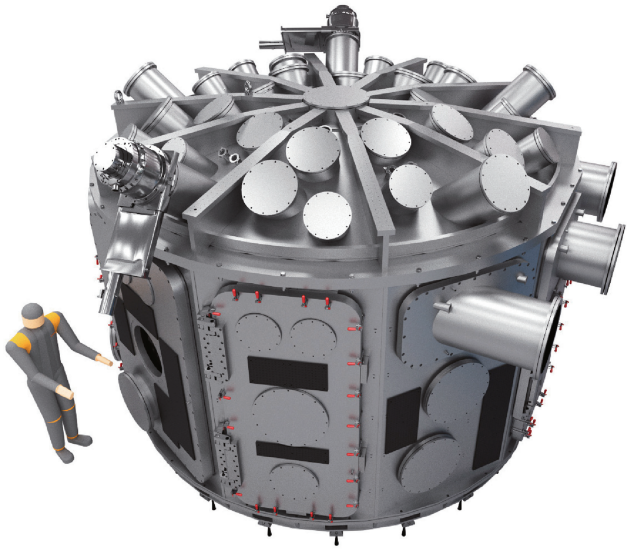

Fig. 16. Design picture of the large vacuum chamber, P3. The chamber has a diameter of 4.5 m, a height of 3.4 m and has a decagonal structure. The volume is approximately 50 m^3. The chamber is supposed to accomodate up to 5 laser beams of variable pulse length and energy at the same time. The small aperture beams enter the chamber in a plane just under the cupola (see the three inlets on the upper right of the picture).

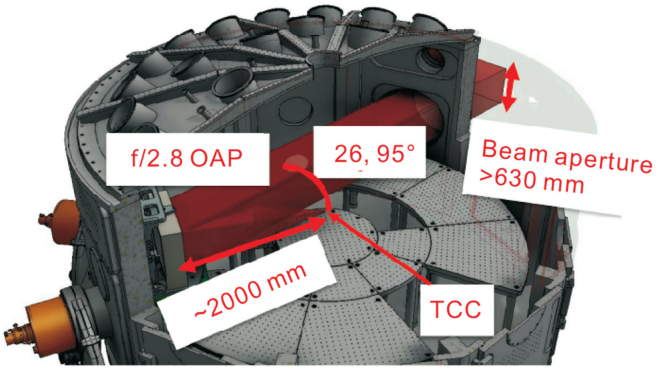

Fig. 17. Focusing geometry of the L4f beam inside the interaction chamber P3 (TCC = target chamber center).

allow for a limited number of energy partitions between the three L4 beams. However, each of them can be at a maximum of 1.5 kJ. The additional small compressor required for the L4p beam is supposed to handle extreme states on a shot-to-shot basis. A fully compressed beam at 150 J and 150 fs will provide an additional 1 PW beam for probing. The other extreme would be 1.5 kJ in several ps. In between these two extremes the energy content and the pulse duration possible depend on the gratings to be used.

High power, high repetition rate solid state lasers with unprecedented parameters are going to become the backbone of the research infrastructure. The Diode Pumped Solid State Lasers (DPSSL) were chosen as the pump technology of the main CPA lasers in the PW and sub-PW class of the ELI-Beamlines facility, while the main amplifiers are using Ti:Sapphire or parametric amplification. The 10 PW class laser operating in the kJ mode relies on progressive Nd:glass flash lamp pumping technologies and direct compression [6].

8.1. The L3 laser (The HAPLS laser system)

The High Repetition Rate Advanced Petawatt Laser System (HAPLS) is designed to deliver PW pulses with energy of at least 30 J and of duration < 30 fs, at a repetition rate of 10 Hz. It is developed by Lawrence Livermore National Laboratory, with ELI-Beamlines cooperating on the development of the PW pulse compressor, of the short-pulse diagnostics and of the short-pulse part controls and timing. The L3 pump engine with design pulse energy of 200 J employs two Nd:glass multislab amplifiers operating at 10 Hz and cooled by He gas at room temperature. Each amplifier is pumped by two high power QCW diode arrays each providing 800 kW peak power; with total power 3.2 MW these are the highest peak-power laser diode arrays in the world. The L3 short pulse part is based on

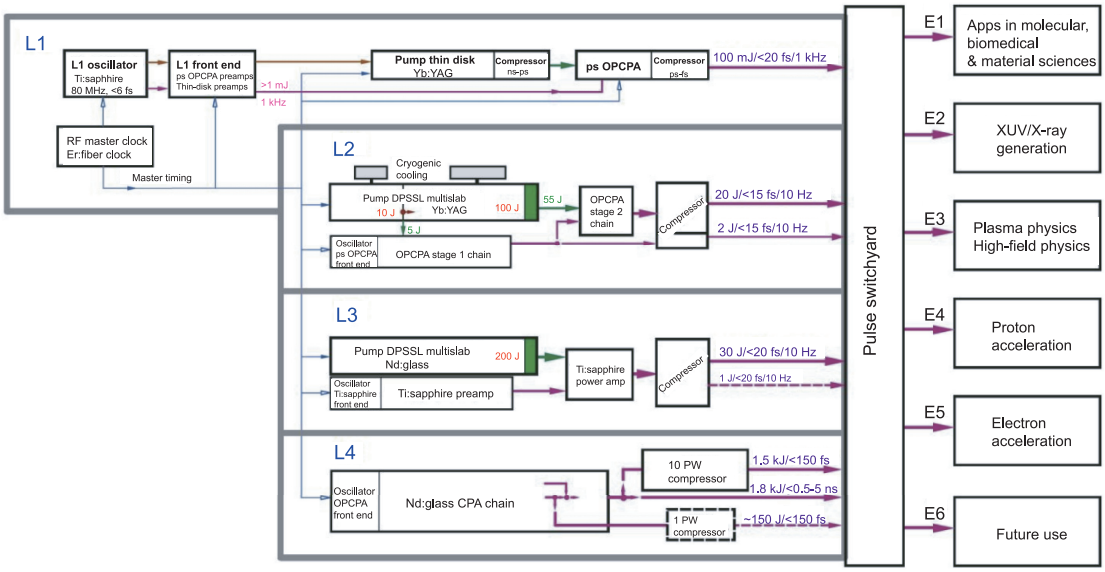

Fig. 18. Master scheme of ELI-Beamlines laser systems. The facility will consist of four lasers, L1, L2, L3 and L4. The L2 scheme is indicated without the long-pulse auxiliary beamline. Considered upgrades for nearest future are indicated by dotted lines. Note that not all lasers go to all experimental halls.

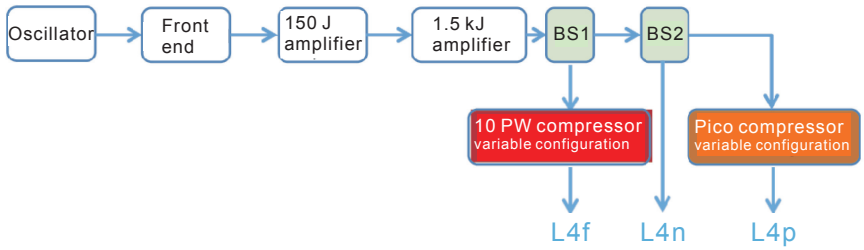

Fig. 19. The conceptual scheme of the L4 beam splitting. L4f is subjected to one reflection, L4p to one reflection and one transmission and L4n to two transmissions.

Table 1
Summary of the laser parameters of ELI-Beamlines. All lasers, except L1, are expected in P3 eventually. The probe beam is expected to be derived from the L3 laser beam. The laser beams L4f, L4p and L4n are derived from the principal laser beam L4 due to double splitting as shown in Fig. 19.

Laser	Energy	Pulse length	Wavelength	Rep. rate
L4n	Max. 1.5 kJ	ns	1057 nm	0.01 Hz
L4p	Max. 1.5 kJ	150 fs −10 ps	1057 nm	0.01 Hz
L4f	Max. 1.5 kJ	150 fs	1057 nm	0.01 Hz
L3	30 J	30 fs	820 nm	10 Hz
L2	15 J	15 fs	820 nm	10 Hz
L1	50 mJ	20 fs	850 nm	1 kHz
Probe	100 mJ	30 fs	820 nm	10 Hz

Ti:sapphire technology, with the output Beta power amplifier cooled by He gas. The pulse compressor unit contains 4 large size 1480 l/mm Au coated gratings. The size of the gratings permits to reach a low average fluence necessary for continuous 10 Hz operation. In order to further limit the risk of grating damage, a contamination getter system is installed between the compressor vessel and the beam distribution system.

The L3 parameters are summarized in Fig. 20 (a) and (b).

8.2. The L4 laser

The L4 laser will provide 10 PW class peak power pulses, with energy of 1.5 kJ and duration 150 fs. It is developed by the consortium National Energetics/EKSPLA, with ELI-Beamlines cooperating on the development of the 10 PW pulse compressor and stretcher, the short-pulse diagnostics, the laser system controls and timing and the design of vacuum vessels. The system employs the approach of mixed Nd:glass, where a sequence of silicate and phosphate amplifiers provides the amplified bandwidth of ~ 13 nm sufficient for compression of the output pulses to < 50 fs. The Nd:glass amplifiers will employ face liquid cooling of the active medium, making it possible to fire a full energy shot approximately every minute. The initial ~ 100 fs pulses are generated in a fiber oscillator, followed by a sequence of OPCPA preamplifiers, stretcher, and pulse cleaner. The high-energy OPCPA preamplifier section boosts the pulse energy to about 4 J and seeds the Nd:glass amplifiers. Upon amplification to ~ 1.8 kJ the pulses are compressed to ~ 150 fs in the 18 m long vacuum

compressor vessel containing four multilayer dielectric gratings with high diffraction efficiency. The pulse compressor is located on the experimental floor while the laser itself is installed in a hall above and the capacitor banks reside in a third room. The L4 architecture makes it possible to generate a non-CPA pulse using a long-pulse narrowband front-end and seed directly the final Nd:glass phosphate kJ amplifier. This non-CPA kilojoule pulse may be generated simultaneously with a CPA pulse of $\sim$ 150 J by using the CPA front-end and amplification chain before the kJ amplifier. The laser is thus able to generate temporally shaped ns pulses synchronized with PW-class pulses with duration of $\sim$ 150 fs.

The most important L4 parameters are summarized in Fig. 20 (c).

9. Some examples of present research of relevance for future experiments

The research activities of ELI cover a wide range. In the following some of the principal actively pursued topics are briefly presented.

9.1. Laboratory astrophysics

Most of the visible universe is in the plasma state. Thus it is highly desirable to performe controlled laboratory plasma experiments (see Fig. 21) which are relevant to the dynamics of astrophysical plasma. Because of the long length scales in astrophysical conditions, dissipation is negligible in the dynamics of the plasma. While the plasma length scales in laser plasma experiments are microscopic ($\lesssim$1 mm), the dissipation can still be neglected in most conditions because of the high temperatures ($>$keV). Thus laser plasma experiments offer the exciting possibility to perform scaled astrophysics experiments with limited similarity [36–38]. These experiments allow the researchers to vary the initial conditions and diagnose the complete time history of an event - aspects which are not possible for most astrophysical plasmas.

The P3 chamber will have a 1.5 kJ beam with a duration of several ns and with programmable intensity. Future upgrades are planned to be able to split it into two beams, an essential requirement for many experiments for e.g., magnetic reconnection [39]. One of the most important benefits of the P3 platform for scaled laboratory astrophysics experiments is the presence of synchronized short pulse beams that can be used for X-ray or proton backlighting. Access to such beams will enable multitude of laboratory astrophysics experiments including those related to driven magnetic reconnection, Weibel instabilities and collisionless shocks [40], plasma jets [41], Kelvin Helmholtz instabilities [42], etc. Pulsed magnetic fields of $<$40 T as described in Sec. 11.1 will also be useful for various laboratory astrophysical experiments. Additionally, future upgrades of the facility will also include access to a probe beam for Thomson scattering (approximately tens of J/ns).

(a)

Parameters	Value	Unit
Beam size (FWHM intensity)	214±5	mm
Beam size (1‰ intensity)	230±10	mm
Clear aperture	250	mm
Beam corner radius	13±3	mm
Beam rotation relative to gravity	0±0.25	deg.
Polarization rotation relative to gravity	0±0.25	deg.
Polarization plane	Horizontal	
λ_0 central wavelength	820 nm	
$\Delta\lambda$ bandwidth (FWHM)	88 nm	
Spectral shape	SG, order 10	
Phase irregularity	<0.25 λ_0	

(b)

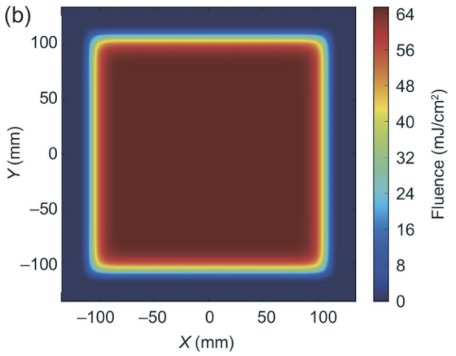

(c)

Parameters	Main beam	Unit
Beam size (FWHM intensity)	582.5±5	mm
Beam size (10^{-3} intensity)	617±5	mm
Clear aperture	650	mm
Beam corner radius	20±3	mm
Beam rotation relative to gravity	0±0.3	deg.
Polarization principle axis relative to gravity	0±0.3	deg.
Polarization plane	Horizontal	
Central wavelength	1057	nm
Pulse duration	<150	fs

Fig. 20. (a) The basic parameters of the L3 laser beam. (b) The spatial profile of the square beam. The intensity follows $I = \exp\left[-2\left(\left(\frac{x}{w}\right)^G + \left(\frac{y}{w}\right)^G\right)\right]$ with $G = 20$, $w = \left(\frac{2}{\ln 2}\right)^{1/G} \times$ FWHM and FWHM = 214 mm. (c) The basic parameters of the L4 laser beam.

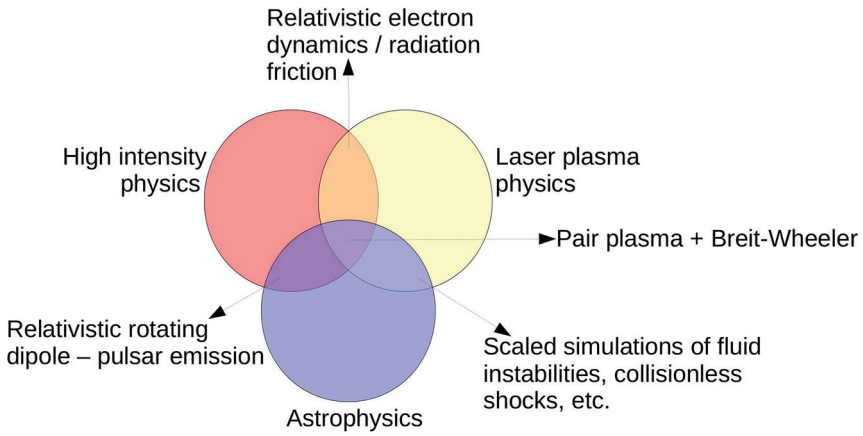

Fig. 21. Various fundamental physical processes have multi-disciplinary applications in astrophysics, high intensity research and laser matter interaction. Some examples are highlighted above and can be studied in a laboratory environment.

In addition to the laboratory experiments enabled by the long pulse (ns) beam, P3 will also have the high intensity 10 PW beam which will provide intensities of the order of 10^{23} W/cm^2 under tight focusing (see Sec. 9.4.2). This intensity regime is expected to lead to several high intensity experiments relevant to astrophysics [10]. Examples include generation of pair plasmas, gamma ray flashes and effect of radiation damping (see Sec. 10.1).

Magnetic reconnection is an ubiquitous phenomea in the universe and its collisonless relativistic version can be investigated in the laboratory. Magnetic reconnection is accompanied by a current sheet formation, where the oppositely directed magnetic fields annihilate. This process has been investigated within the framework of dissipative magnetohydrodynamics [43]. However, in relativistic conditions, it changes character due to the relativistic constraint on the particle velocity which never exceeds the speed of light in vacuum. In our recent research using 2D Particle-in-cell (PIC) simulations, we have found that fast relativistic magnetic annihilation is achieved with two parallel ultra-short petawatt laser pulses co-propagating in an underdense plasma (see Fig. 22 (a)) [44,45]. The two magnetic dipoles generated by the laser pulses annihilate in the current sheet formed at the central axis. According to the Ampère-Maxwell equation, $\nabla \times \boldsymbol{B} = \mu_0 \boldsymbol{J}_\mathbf{e} + \mu_0 \varepsilon_0 \partial \boldsymbol{E}/\partial t$, the magnetic field variation is balanced by the electron current and the displacement current in the current sheet. Due to a low plasma density and an upper limit for the electron velocity, the variation of the magnetic field can only be compensated by the displacement current, which induces an electric field and accelerates the charged particles in the current sheet (see Fig. 22 (b)). From a series of simulations and analytical works, we found that with laser pulses reaching the intensity of 10^{23} W/cm^2 it is possible to realize the relativistic magnetic reconnection in near-critical or overdense plasma, which provides more efficient particle acceleration by the inductive electric field [46]. Our results open a new way for understanding relativistic regimes of fast magnetic field dissipation, where the large-scale magnetic field energy is converted to the energy of collimated bunches of fast charged particles. It also provides a basis for the future experiments. When two intense femtosecond laser pulses are well synchronized, the above-discussed regimes can be realized with a gas jet or an easily available foam targets.

9.2. Warm dense matter

The long and short pulse laser beams in the P3 interaction chamber can be used to produce secondary radiation and particle beams which will be utilized as diagnostic probes for studying exotic states of matter. Quasi-monoergetic X-ray sources can be produced by K_α-radiation driven by suprathermal electrons in fs laser interaction with solid targets or by

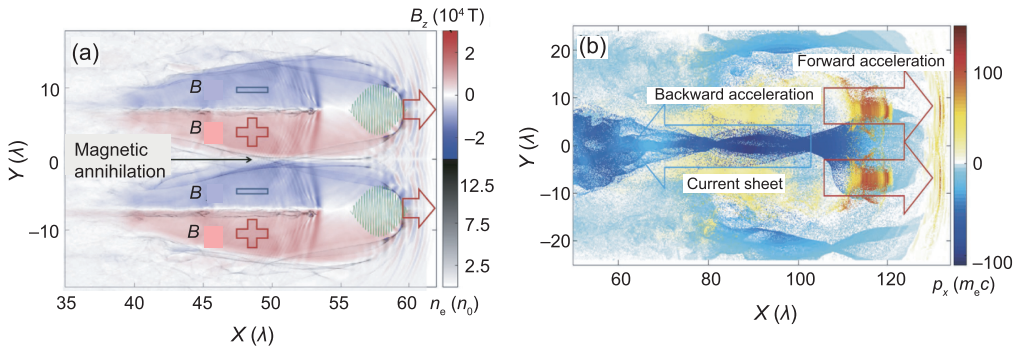

Fig. 22. (a) Magnetic dipoles and electron density. (b) Electron backward acceleration in the current sheet.

atomic transitions in He- and H-like atoms in solid foils thermally ionized by long-pulse lasers with ns duration [47,48]. We are also testing various nanostructured targets for more efficient K_α production by short-pulse lasers [49,50]. The laser-driven K_α emission has significantly lower conversion efficiency than conventional He_α sources, but has the advantage of shorter duration, i.e. better temporal resolution, and narrow line profile [51]. It is expected that lines K_α yield can be enhanced, possibly by a whole order of magnitude, thanks to the strong electric fields created in the cavities within the nanostructured target that allow more fast electrons to move through the target and create inner-shell emission at higher intensity. This diagnostic would be perfect for the ELI Beamlines facility which has access to a short-pulse kJ L4f laser with a good temporal contrast.

Ion or proton beams can be generated on thin foils via TNSA or other acceleration schemes [52]. Such proton sources are already well established in the field and we plan to implement these standard techniques in the P3 interaction area as well. Laser Wake Field Acceleration (LWFA) can produce quasimonoenergetic and highly directional electron beams with energies varied from one till hundreds MeV [53]. If the source is tuned to the lower range of electron energies in the downramp LWFA regime, these can be used for electron diffraction or scattering [54–56]. If it is tuned to higher energies, it produces the broadband soft X-ray betatron beam described in a separate section. Production of energetic neutron sources from interactions of ultra intense short pulse lasers with thin targets based on relativistic transparency has been demonstrated as viable diagnostic technique [57,58]. Thanks to an expected high contrast, short pulse duration and high energy of the L4 beamline we expect to be able to drive energetic neutron beams at high yield. This system in the P3 area is capable of boosting the present neutron production records by at least two orders of magnitude, opening new experimental setups. Moreover the high repetition-rate systems at ELI Beamlines allow for the transition of the groundbreaking fundamental research to real applications including fast neutron radiography, active interrogation of nuclear materials, neutron resonance spectroscopy and other.

Warm Dense Matter (WDM) is a unique state of matter (see Fig. 23) common to many astrophysical objects such as planetary cores, brown dwarfs, or crusts of old stars [59]. WDM is readily created in interaction of energetic lasers with solids and it is a transient state during the inertial confinement fusion (ICF) implosions [60,61]. WDM state is defined by moderately high temperatures of $0.1 - 100$ eV, solid densities, and pressures above 1 Mbar. In this state, ions are strongly correlated and the electron population is partially or fully degenerate making the theoretical description of WDM very challenging and thus requires a very thorough experimental verification [62,63]. The P3 experimental area at ELI Beamlines provides a unique platform for many different ways to study the structure and thermodynamic properties of WDM under controlled conditions. The very specific combination of short and long pulse lasers as well as external magnetic field generator [64] will enable both novel techniques to create and study WDM, but also combination of experimental techniques and multiple diagnostics not possible in more traditional facilities. In addition, high repetition rate will be beneficial to efficient data acquisition during these experiments, which is particularly interesting for diagnostics with weak signals such as X-ray Thomson scattering (XRTS) [51] or absorption spectroscopy using the betatron source [65].

Shock or ramp compression with laser drivers is used to create very dense heated states of matter in the WDM state both from solid density targets as well as cryogenic samples or low density foams and aerogels [66–68]. The capabilities for handling of cryogenic targets are foreseen for the ELI Beamlines facility. Another way to create WDM states is the laser-driven shock-and-release method [69]. Short-pulse lasers can be used to create dense heated states by isochoric or volumetric heating using laser X-rays [70] or protons [52]. These sources can then be used both for probing and pumping purposes on femtosecond time scales. This will allow us to heat or ionize any material on time scales shorter than thermal motion or hydrodynamic expansion as well as probe non-equilibrium dynamics of WDM.

In order to carry out the comprehensive characterization of the thermodynamic state, structure and transport properties of WDM, we will need a large scope of different diagnostics at our disposal. Many of the standard diagnostics will have to be implemented at ELI Beamlines. One of the most important examples of crucial diagnostics is velocity interferometry (VISAR) used to measure velocities of dense shockwaves [71]. This instrument consists of a probe optical laser that reflects from the moving shock front that becomes conductive and thus

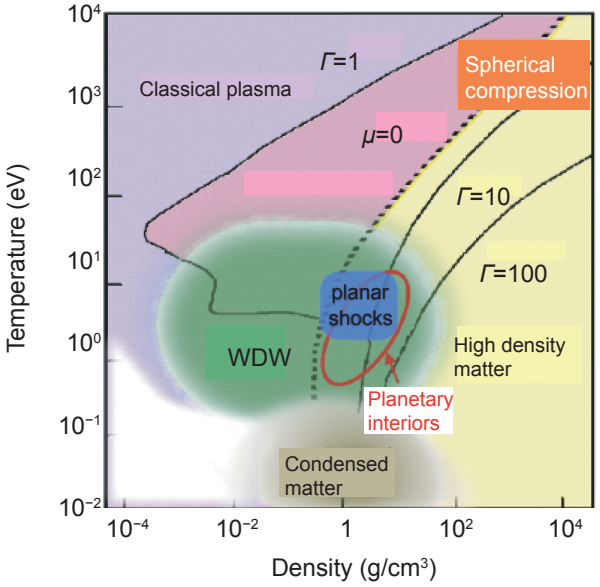

Fig. 23. Temperature-density phase diagram. WDM lies between condensed matter, hot dense matter and ideal plasma, and overlaps the planar laser generated shocks in matter as well as the astrophysical conditions. Γ is the coupling parameter (ratio of Coulomb and thermal energies). The $\Gamma = 1$ line separates the strongly and weakly coupled regimes and μ stands for the chemical potential where the $\mu = 0$ line signifies the area where the Fermi energy equals $k_B T$, i.e. fully degenerate matter.

reflective. Using an interferometer coupled with an optical streak camera a phase difference from the Doppler shifted reflected laser provides the velocity, from which pressure and density of the shock front can also be calculated using the Hugoniot relations. Streaked optical pyrometry (SOP) is then used for temperature measurements in shockwaves or in plasmas heated through other processes [72]. Another standard diagnostic used particularly to study density fluctuations envisioned for these experiments is X-ray radiography [47]. The X-ray sources can be driven by short and long pulse lasers. Similar sources can also be used for X-ray diffraction [73]. We will also implement proton radiography, which can be very useful for the ultrafast applications [74]. Density fluctuations can also be studied with X-ray Phase Contrast Imaging (PCI) with excellent spatial resolution [75], which is also going to be implemented on laser driven X-ray sources with varying temporal resolution (ns to tens of fs). These diagnostics all have their limitations and none of them is capable of providing direct or full measurement of transport, structure or EOS in WDM samples, but they will provide important complementary information needed to make a completely model-independent measurement of the thermodynamic state of WDM.

XRTS has become a widely used diagnostic for the study of WDM as it is capable of providing a simultaneous and direct 'in-situ' measurement of electron temperature, density, ionization state and the microscopic properties of dense plasmas [51,76]. Simultaneous collective and non-collective XRTS measurements will be available. The ELI Beamlines team is developing a set of X-ray crystal spectrometers with excellent spectral and spatial resolution necessary to resolve XRTS from various parts of the targets. For this purpose, we will design a special toroidally or spherically bent crystal for specific X-ray energies (~ 9 keV, Cu K_α source, or higher for higher Z samples). We will couple it with a deep depletion in vacuum CCD camera or Image Plates. The efforts of the development of nanostructured targets for more efficient K_α production by short-pulse lasers is instrumental to successful implementation of the XRTS technique as a standard diagnostic technique at ELI Beamlines [49,50]. In order to study the non-equilibrium dynamics in WDM, we are also developing ultra-fast electron and X-ray probes based on LWFA for absorption spectroscopy and electron diffraction [53−56] (see betatron section below). The multi-beam capability of the facility in conjunction with a very large and versatile interaction chamber can then accommodate a very large number of different setups ranging from relatively simple geometries with single targets to very sophisticated experiments with multiple beams and complicated 3D geometries. An example of one of the more complicated setups with several laser beams and combination of diagnostics is shown in Fig. 24.

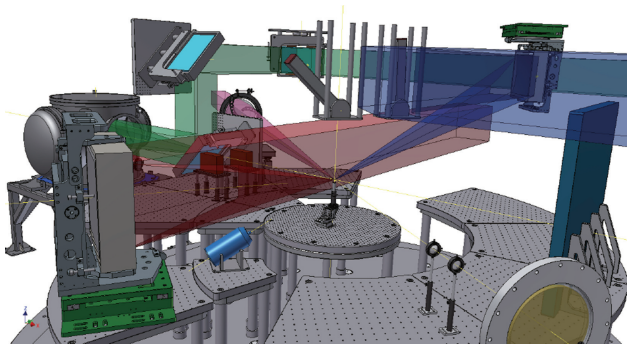

Fig. 24. A schematic of a potential layout for a sophisticated experiment to study WDM. A long pulse beam (ns duration) is used to drive a shockwave in a planar sample, while another ps-beam irradiates a thin foil from above producing X-rays for radiography which are detected transversally by a film pack below the target. The kJ short pulse beam is used to drive a K-α source for simultaneous collective and non-collective XRTS detected by two curved crystals mounted from the upper breadboard inside the chamber. The shock velocity and self emission of the shockwave is recorded by VISAR and SOP diagnostics setup on an optical table outside the chamber (not shown in the diagram). Additional betatron diagnostic using a 30-fs beam focused inside an external chamber is also shown.

9.3. Laser-plasma interaction for inertial confinement fusion in the context of the shock-ignition approach

Inertial confinement fusion (ICF) for energy remains an important topic of worldwide efforts [77−79]. Several approaches are under consideration, such as direct drive, indirect drive [22], and various forms of fast ignition. More recently, a new approach was suggested: shock ignition [80−84] (SI). However, the underlying principles of shock-ignition have a rather long history [85−87]. Similar to fast ignition, shock ignition decouples compression and fuel assembly from ignition by basically redistributing the available energy in the drive, see Fig. 25(a). The peak at the end of the compression phase poses particular problems in the context of laser−plasma interaction as the intensity is rather high and pure hydrodynamic modelling is questionable. Over the last 10 years considerable effort has been put into understanding better laser−plasma interaction in the context of shock ignition [23,24,88−94] (and many references therein).

Laser-plasma interaction for ICF conditions still poses many problems on the macroscopic level as much as on the microscopic level. Two of the most pressing issues are transport and absorption. Transport around the critical density is non-local for particles as well as radiation. This means that the mean-free-path (mfp) of the transported quantities is larger than the typical gradient scale-length (see Fig. 25(b)). This changes completely the energy fluxes and correspondingly the plasma state. Correct macroscopic/hydrodynamic modelling requires that the transport coefficients are modified, accounting for kinetic effects. Transport is a strong function of the so-called Knudsen number, which is defined as:

$$K_n = \frac{\lambda}{L}; \quad L = \frac{T_e}{|\nabla T_e|}. \tag{2}$$

Here, λ is the mfp for the particles, L is the typical gradient scale length affecting the particle transport and T_e is the electron temperature. Simulation codes need to be developped which handle nonlocal transport correctly (see [95−97] and many references therein). Fig. 26 gives an example on the strong variation of the Knudsen number from the plasma

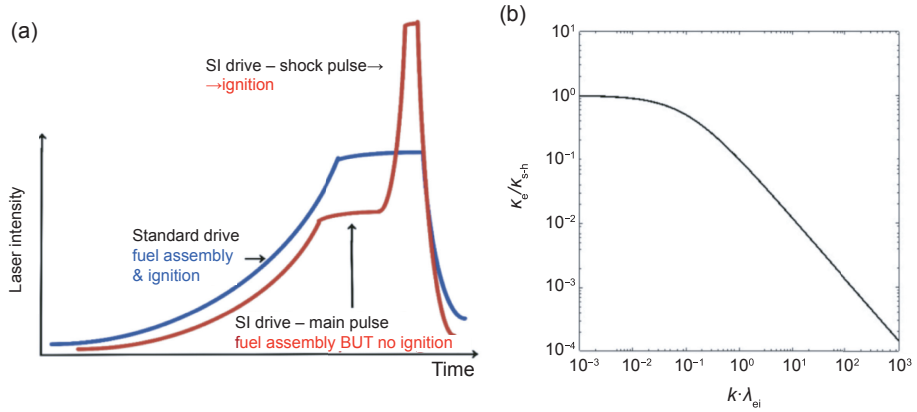

Fig. 25. (a) Evolution of the intensity in the case of conventional drive (blue curve) and SI drive (red curve). In conventional drive fuel assembly and high velocity are achieved, creating a hotspot and ignition. In contrast, in SI the main drive is responsible for fuel assembly but not for ignition. The short high-intensity shock-inducing pulse launched at a later time will reach the fuel at stagnation and ignite it. (b) The typical variation of the electron heat flux conductivity (normalized to the corresponding Spitzer-Härm conductivity) as a function of the electron mean-free-path.

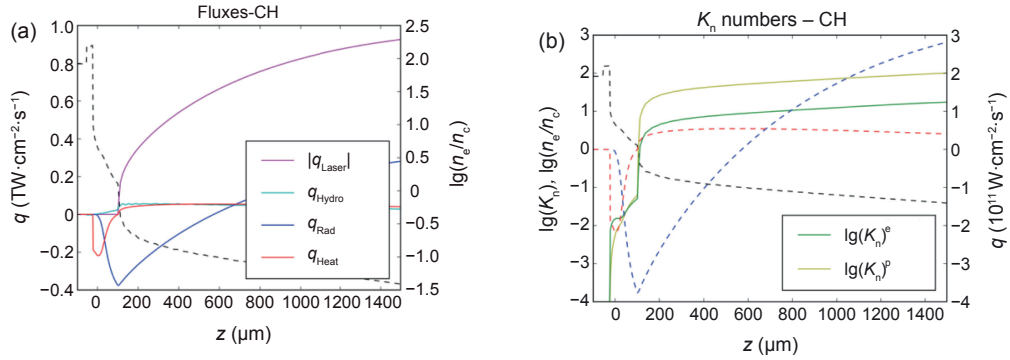

Fig. 26. (a) Fluxes and corresponding Knudsen number for a solid CH target due to laser-induced ablation. K_n^e and K_n^p are the Knudsen numbers for electrons and photons, respectively. The dashed black line in (a) and (b) shows the resulting plasma density profile. The various fluxes shown in (a) are reproduced in (b) with the same color coding.

corona, via the critical density layer into the shock-compressed matter.

Kinetic effects are not only important for transport processes but also (in particular at high laser intensities such as in shock-ignition) for absorption processes in the plasma corona, e.g. around the quarter-critical density $n_c/4 \approx 0.25 \times 10^{21}/\lambda_o^2$ (cm^{-3}) (with λ_0 in μm), see Fig. 27. Absorption is given not just by inverse Bremsstrahlung in the vicinity of the critical layer but throughout the plasma corona due to the excitation of collective effects driven by parametric instabilities such as Raman backscattering, Brillouin backscattering, two-plasmom decay instability and others. These processes are important as they determine also the hot electron production. Depending on their distribution function they might be beneficial for driving shocks or detrimental as they can induce preheat of the compressed fuel (two recent reviews consider in some details parametric processes for ICF using kinetic simulations [23,24] and detailed references therein).

Kinetic simulations in 3D for plasmas of hundreds of microns and tens of picosecond duration are prohibitive. It is therefore necessary to develop new sophisticated simulation tools where important kinetic effects for transport and absorption are incorporated in order to have viable tools for predictive simulations.

9.4. Plasma optics

Plasmas are a powerful medium to manipulate coherent light [25,98]. It can be used to amplify laser pulses (see Sec. 9.4.1 below), to diffract [99] them, to clean them [100] and to focus them (see Sec. 9.4.2). A plasma can be considered as a transient optical element, which is, however, basically stationary on the time scales of ultra-short laser pulses (tens to hundreds of femtoseconds). Plasmas most likely will play an important role to pave the way towards exawatt laser systems.

9.4.1. Plasma amplification using ion modes

The original idea of plasma amplification to compress laser pulses goes back a long time [101–105]. Parametric instabilities in a plasma, like stimulated Raman scattering (SRS)

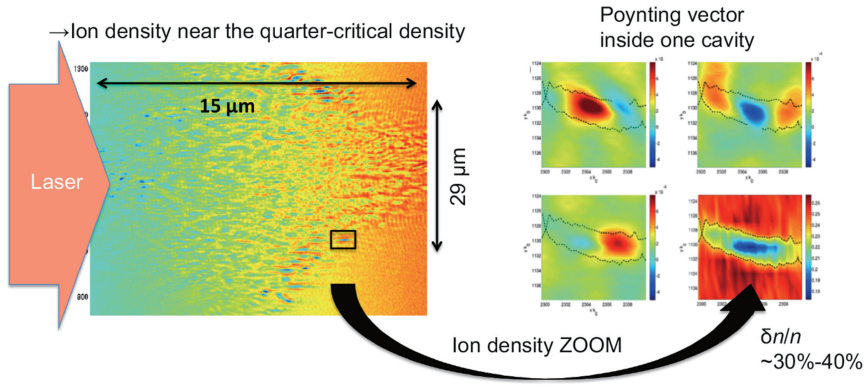

Fig. 27. An example of the complexity of the absorption process in the vicinity of the quarter-critical density. An intricate interplay of many parametric instabilities determines the absorption of the laser beam and the production of hot electrons. Even solitonic structures of limited lifetime play a role. The important conclusion is that for SI a substantial amount of the incident laser energy can be absorbed in the plasma corona rather than at the critical density. This affects the shock generated.

or stimulated Brillouin scattering (SBS), present the coupling between two transverse electromagnetic modes (the lasers) and a longitudinal compressional mode (the plasma). The plasma mode can be taken up either by the electrons or by the ions. Only ion-based modes are considered here. The idea of plasma amplification is to exploit this process in a controlled way. The basic principle of plasma amplification is shown in Fig. 28. Two laser pulses, a long pump pulse and a short seed pulse, collide in a plasma and energy transfer takes place. In the ideal case the pump is depleted and the intensity of the original seed pulse is increased correspondingly. The seed pulse provides the characteristic time-scale of the final result. The energy transfer becomes possible as the beating of the two electromagnetic modes sets up a plasma grating [26,106] which scatters the pump pulse into the seed pulse.

The possible characteristic time scales a plasma can support depends on the growth rate of the mode and the seed pulse duration. If the seed is shorter than the inverse growth rate, amplification becomes difficult or fails. In general electron plasma modes have a much shorter time-sccale than ion-based

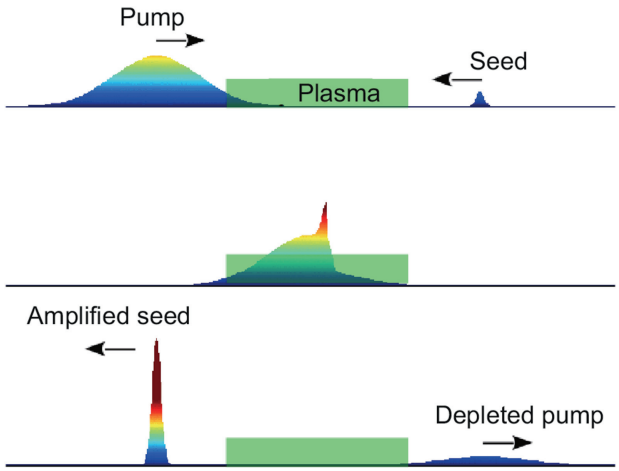

Fig. 28. Cartoon of the basic principle of plasma amplification. A pump pulse and a short seed pulse collide inside a sub-critical plasma and energy transfer is initiated due to parametric backscattering processes.

modes. However, if one puts oneself in the so-called strongly-couples regime of SBS (sc-SBS) [107] then seed pulse durations of a few tens of femtoseconds can be handled. This strongly coupled regime of Brillouin backscattering is described by a quasi-mode, which is driven by the local laser intensity rather than being an Eigenmode of the plasma. The corresponding dispersion relation is given as:

$$\omega = \omega_{\mathrm{sc}} + \mathrm{i}\gamma_{\mathrm{sc}} = \left(\frac{k_{0\mathrm{p}}^2 v_{\mathrm{osc}}^2 \omega_{\mathrm{pi}}^2}{2\omega_{0\mathrm{p}}}\right)^{1/3}\left(\frac{1}{2}+\mathrm{i}\frac{\sqrt{3}}{2}\right). \tag{3}$$

Here, ω_{pi} is the ion plasma frequency, $\omega_{0\mathrm{p}}$ the pump laser frequency and v_{osc} the quiver velocity of the electron in the laser field. This mode therefore depends directly on the laser intensity.

A threshold condition determines whether one operates in the sc-SBS regime:

$$\left(\frac{v_{\mathrm{osc}}}{v_{\mathrm{e}}}\right)^2 > 4k_0 c_{\mathrm{s}}\frac{\omega_{0\mathrm{p}}}{\omega_{\mathrm{pe}}^2}. \tag{4}$$

c_{s} is the standard ion-acoustic velocity and ω_{pe} the electron plasma frequency.

The strong coupling regime of Brillouin backscattering is characterized by density perturbations $N = \delta n/n_0$ which vary strongly over an acoustic period. Therefore the second derivative in the plasma response needs to be retained in order to describe correctly the temporal evolution of the plasma response. The coupled set of 3-wave equations is the following:

$$\begin{aligned}
\left(\partial_t + v_{\mathrm{g}}^{\mathrm{p}}\partial_x\right)E_{\mathrm{p}} &= -\mathrm{i}\frac{\omega_{\mathrm{pe}}^2}{4\omega_0}NE_{\mathrm{s}}\mathrm{e}^{-\mathrm{i}(\omega_{0\mathrm{s}}-\omega_0)t},\\
\left(\partial_t - v_{\mathrm{g}}^{\mathrm{s}}\partial_x\right)E_{\mathrm{s}} &= -\mathrm{i}\frac{\omega_{\mathrm{pe}}^2}{4\omega_{0\mathrm{s}}}N^*E_{\mathrm{p}}\mathrm{e}^{-\mathrm{i}(\omega_0-\omega_{0\mathrm{s}})t},\\
\left(\partial_t^2 - c_{\mathrm{s}}^2\partial_x^2\right)N &= -\frac{2Ze^2}{m_{\mathrm{e}}m_{\mathrm{i}}c^2}E_{\mathrm{p}}E_{\mathrm{s}}^*\mathrm{e}^{-\mathrm{i}(\omega_0-\omega_{0\mathrm{s}})t}.
\end{aligned} \tag{5}$$

Here, $E_{\mathrm{p,s}}$ are the electromagnetic field perturbations of pump and seed, respectively. A limiting condition for the

intensity of the amplified seed is given by wave breaking. Wave breaking destroys the plasma Bragg grating and terminates the energy transfer. On the other side a seed pulse shorter than γ_{sc}^{-1} will not be amplified either. Depending on the plasma density used, the intensities will be limited to something of the order of 10^{18-19} W/cm^2. The idea is to go transverse and have large focal spots. Plasma focusing will then provide the final extremely high intensities as shown in Fig. 29.

Plasma amplification uses a medium which is already broken down and can therefore sustain very high energy densities. It might be a way to overcome the limitations of solid-state based optical material which are subject to the damage threshold given by ionization [108]. Plasma amplification in the sc-SBS regime has received a lot of attention in the last few years [109–120] and proof-of-principle experiments have been carried out very successfully [121,122].

Although in principle a very simple configuration, the actual optimization is challenging as competing parametric processes exist [110] and the detailed role of chirp, energy flow directionality and amplification optimization are nontrivial [114, 115].

9.4.2. Plasma-based tight focusing

The standard mode of operation of the 10 PW laser at ELI Beamlines will include an OAP (off-axis parabola) with *f*-number 2.5 – 2.8. Under these conditions, the paraxial approximation will be valid to describe the focused beam and the achievable intensities will be $>10^{22}$ W/cm^2. However, there is consistent effort to push the achievable intensities by an order of magnitude where many novel processes like radiation reaction, electron–positron pair creation, dominance of radiation pressure over the thermal pressure of plasma and even relativistic ion motion will be dominant [10,18]. This completely changes the process of conventional laser–matter interaction and a new era of physics discoveries is expected (see Fig. 30).

Traditionally higher intensities on existing facilities are achieved using a small *f*-number parabola [123] or an ellipsoidal plasma mirror (EPM) [124–127] (see Fig. 32). Because of debris damage and the associated financial implications,

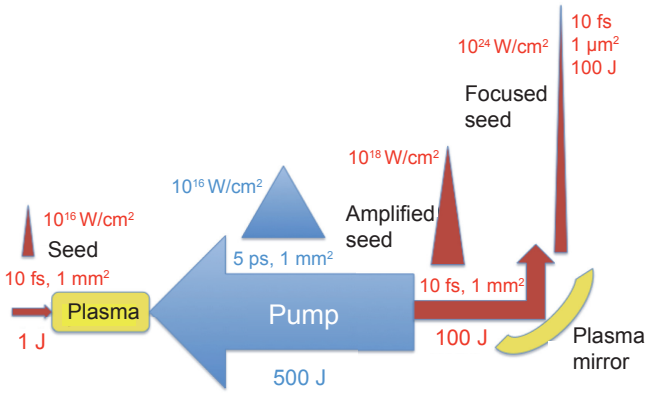

Fig. 29. Principal idea to obtain extremely high intensities using plasma amplification and plasma focusing.

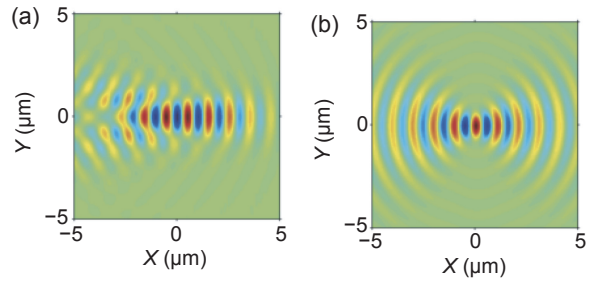

Fig. 30. A particle-in-cell simulation of a laser pulse focused down to a spotsize of 1 μm. (a) Using the paraxial approximation and (b) using the correct tight focusing approach. The time reversability of the Maxwell equations is violated in the paraxial approximation. Describing correctly tight focusing requires substantial modifications of the boundary conditions in kinetic simulation codes.

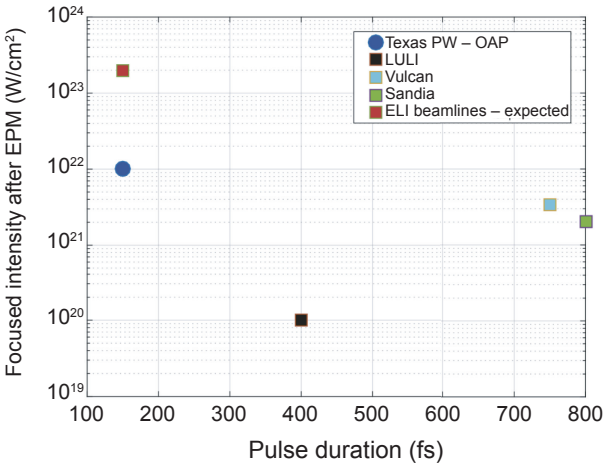

Fig. 31. The parameter space of focused intensity and pulse duration for the experiments using EPMs and tightly focused OAP (only for $I>10^{21}$ W/cm^2). Squares represent EPM experiments that have been done [126,127], and circles represent the parameters of tightly focused OAP. The value for the Texas PW stems from an approximate estimate based on typical laser parameters in conjunction with a f/#1 OAP.

using a small f-number parabola is not a viable option for the 10 PW laser at ELI Beamlines. The technology for using the EPMs for the parameters of the 10 PW beam in an cost effective way is being researched at ELI Beamlines.

Fig. 31 shows the parameter space of previous high intensity experiments using the EPMs and a tightly focused OAP. It also shows the expected parameters achievable with the 10 PW beam at ELI Beamlines. In preparation for such experiments, preliminary test-experiments are planned on existing facilities which provide pulse durations of the order of ~ 100 fs and at the same time theoretical tools are being developed to model the beam parameters under tight focus [128,129].

The combination of a standard OAP with an EPM (Fig. 32) for refocusing is the most likely approach to achieve UHI in a controlled way. The EPMs have to be replaced after each shot and ways are investigated to produce them cheaply.

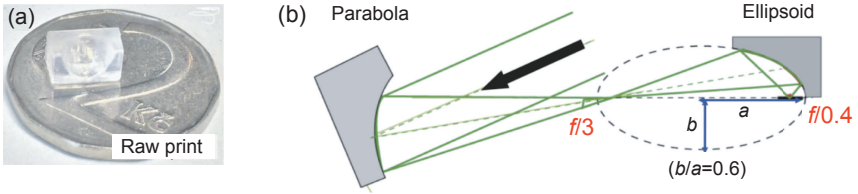

Fig. 32. Example of (a) an ellipsoidal plasma mirror and (b) a possible focusing geometry based on the combination of an OAP and an EPM of very different *f*-number.

10. High-field interaction

10.1. Some aspects of high-field physics

The high intensity $I \gtrsim 10^{22}$ W/cm^2 regime enables studying highly non-linear mechanisms of interactions of energetic particles with intense fields [130]. Among others, production of a "secondary source" of γ-radiation created during the interaction of ultra-intense laser pulse with matter due to radiation reaction [131] is of particular interest. It allows not only to test the fundamental physics theory of radiation emitted by accelerated charged particle and its back-reaction on the dynamics of the particle itself but also to develop laboratory γ-ray sources for radiography in material and biological sciences, treating some forms of cancer, removal of bacteria, or scanning shipment containers [132]. Studying laboratory γ-ray flashes could also provide insight into complex astrophysical phenomena where such flashes occur as signatures of cosmic ray acceleration at shock wave fronts, or emissions from pulsars, where γ-rays are generated via bremsstrahlung, pion decay, inverse Compton scattering, and synchrotron radiation of ultra-relativistic electrons rotating in magnetic fields [133–139].

To generate hard X-rays and γ-rays at lower laser intensities, one can also use relativistic electrons coming from a laser-wakefield accelerator. Several recent experiments focused on all-optical radiation generation from laser-electron scattering [140–144]. High-energy photons were created, but the total energy emitted by the electrons during the interaction was still negligible compared with the initial electron energy content. At somewhat higher laser intensities ($I \geq 10^{21}$ W/cm^2), the electron energy loss due to radiation reaction in the laser - electron scattering can become relevant [145,146]. Even though a GeV-class electron beam could lose up to 50% of the total energy, this is accomplished through repeated emissions of low-energy photons, which is expected to be well-described by the semi-classical Landau and Lifshitz equation of motion. However, if a single photon emitted carries a significant percentage of the electron energy, then quantum treatment is necessary. The parameter, which decides whether the radiation reaction is classical or quantum $\chi_e = \sqrt{\left(p_\mu F^{\mu\nu}\right)^2}/(E_S m_e c)$, is the field strength in the frame of the moving charge normalized to the Schwinger limit field $E_S = m_e^2 c^3/(e\hbar)$ [147]. Here p_μ is the particle 4-momentum, $F^{\mu\nu}$ the electromagnetic tensor and other symbols have their usual meaning.

Quantum-dominated radiation reaction exhibits distinct features compared with the classical radiation reaction. The intrinsically stochastic nature of the emission influences the electron beam divergence, energy spread and the direction of radiation emission [148–152]. These features can be measured in experiments with the new generation of lasers, such as the ones to be available at ELI Beamlines. At laser intensities of $I \geq 10^{23}$ W/cm^2 the electromagnetic radiation interaction becomes highly dissipative due to the emission of γ photons. The high energy photons can decay in the strong EM field producing electron–positron pairs, which in turn will lose their energy emitting photons [153]. Studying the spectra of γ photons produced during such high-energy interactions will provide invaluable insight into the nature of electromagnetic interaction beyond the classical limit of weak fields.

In the interaction of an ultra-intense laser pulse with a solid target, the radiation due to acceleration of electrons in the laser field is competing with the radiation due to scattering of electrons in the Coulomb field (bremsstrahlung) and it is necessary to study signatures of both of them to be able to distinguish them in experiments. The radiation reaction has to be treated self-consistently in numerical simulations because it has an effect on the dynamics of the interaction itself. Fig. 33 shows the snapshot from the interaction of a 30 fs laser pulse with the intensity 10^{22} W/cm^2 with solid density plastic foil target (the laser propagates from left to right). The photons are generated in front of the target where the target surface is deformed by hole boring. The efficiency of this process thus depends in particular on the conditions of the interaction at the target surface. Bremsstrahlung radiation on the other hand originates inside the target and it strongly depends on the target material and thickness. In experiments with solid target it is possible to suppress bremsstrahlung emission by using thin targets of low Z material in which case the dominant source of γ photons should be due to radiation reaction. Radiation reaction efficiency increases with the laser pulse intensity much more strongly and it is the dominant source of γ photons for the intensity of 3×10^{22} W/cm^2.

In the high field region, the interaction of laser wave with relativistic particles is accompanied by another quantum electrodynamic effect, electron–positron pair creation due to Breit-Wheeler process [154]. Similarly to emission of γ photons, this process is governed by the parameter $\chi_\gamma = \hbar\sqrt{(F^{\mu\nu}k_\nu)^2}/(E_S m_e c)$, where k_ν is the four-momentum of a photon having the angular frequency ω_ν and the wave vector $\boldsymbol{k}_\nu$. Previously, electron–positron pairs have been

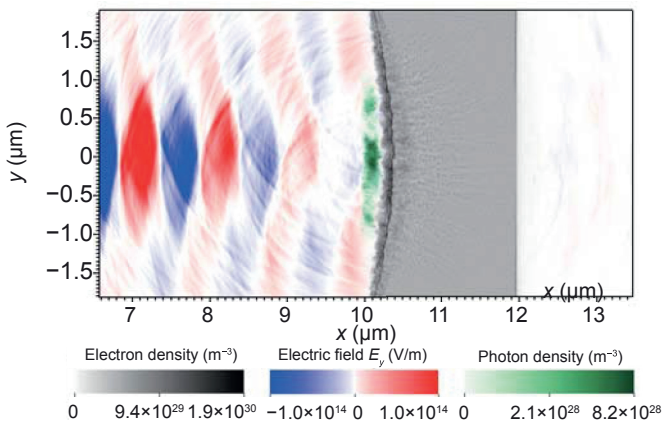

Fig. 33. A 30 fs laser pulse (coming from the left) interacting with electrons on the front side of a thin foil. The process generates high-energy photons. Grey color shows the electron density while the density of the high-energy photons is given in green. The red-blue scale shows the transverse component of the laser field.

produced in experiments with moderate laser intensity and a counter-propagating ultra-relativistic (46 GeV) SLAC electron beam [155]. A high value of quantum parameter χ_e and χ_γ was achieved due to the extremely energetic electron beam. As a consequence, the experiment was operating in a quantum regime despite the moderate laser intensity. However, this setup produced a very low number of pairs, since the pair creation rate was low. A similar setup relying on a 1 GeV-class electron beam and an extremely intense laser (Fig. 34) has a potential to produce a much higher number of electron–positron pairs and allows for all-optical configuration in which the electron beam is accelerated by the laser pulse.

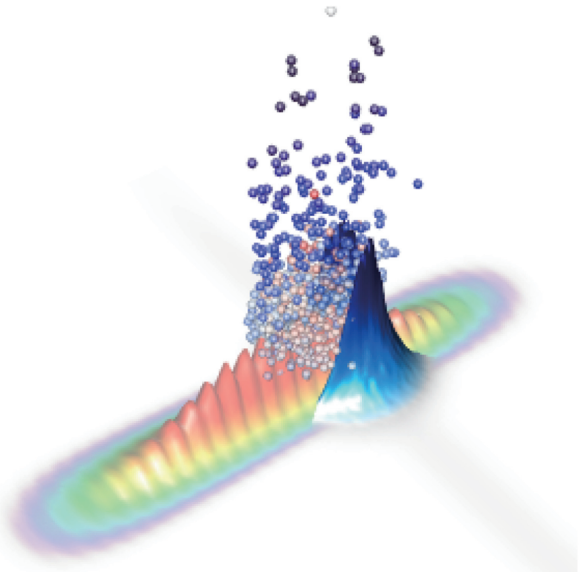

Fig. 34. Pair creation in laser-electron beam scattering. The blue surface represents the interacting electron beam density, while the newly generated pairs are shown as individual particles.

The most promising setup leading to a prolific pair production is the electron–positron pair generation in an electromagnetic standing wave formed by two colliding laser pulses of equal amplitudes and frequencies [156]. In this configuration, seeding electrons are trapped in the position of the electric field antinode, i.e. where the electric field has its maximum amplitude. That leads to efficient γ-ray radiation and pair production since both parameters, χ_e and χ_γ, depend on the strength of the electromagnetic field. The results suggest that the intensity required for cascade pair production is of the order of 10^{24} W/cm^2 which is two orders of magnitude lower than the threshold for self-seeded cascades when two colliding laser pulses are used [157].

Nevertheless, the efficiency of γ-ray radiation and pair production in the standing wave [158] depends on laser polarization and the cascade seeding. The highest efficiency of a circularly polarised standing wave is achieved when the seeding electron is placed precisely at the electric field antinode, since the electron emits photons as it rotates in the same sense as the standing wave does. Otherwise, due to the ponderomotive force the seeding electrons are expelled from the high field region to the nodes where they are trapped. In the case of a linearly polarized standing wave, electrons quickly depart from the electric field antinodes to nodes. Therefore, photons and pairs are mainly generated at the position of electric field nodes as depicted in Fig. 35.

A linearly polarized standing wave is more favourable for γ-ray radiation and pair production since electrons oscillate between nodes and antinodes resulting in a periodic emission. The intensity threshold for pair production can be lowered by using a target that provides multiple seed electrons [159], or using a multiple-laser beam configuration [160,161]. It has been found, that the cascade pair production can develop when eight pulses, each of intensity 10^{23} W/cm^2, are used [160].

More exotic effects due to laser–matter interaction, such as gravitational wave generation [162], are in principle possible, but present-day diagnostics are not yet sensitive enough.

10.2. High-field diagnostics with X-ray spectroscopy

The investigation of exotic states of the matter can be used for the development of alternate X-ray diagnostic methods applicable at extremely high laser intensities. The high-resolution X-ray spectroscopic measurements will concentrate on the identification and interpretation of exotic radiative phenomena connected with the interaction of highly relativistic laser beams with solid and gas targets. The emission spectra at photon energy larger than approximately 20 keV will be recorded using the Laue type diffraction at cylindrically bent crystals, and the investigation of less energetic X-ray spectra will be based on 2D-bent Bragg type crystals. The first experiments using the latter type of spectrometers will investigate the effects of hot electrons on intensity redistribution and profile modification of emitted spectral lines. While at sub-relativistic laser intensities the characteristic energies of hot electrons generated due to strong parametric instabilities (stimulated Raman scattering, and two-plasmon

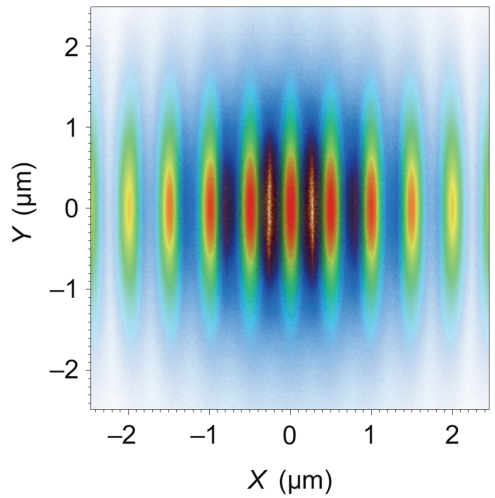

Fig. 35. Generation of photons (blue) and Breit-Wheeler electrons (orange) at the electric field nodes in the linearly polarized standing wave originating from the collision of two laser pulses.

decay processes) typically achieve tens of keV [82], and at intensities above 10^{20} W/cm^2 the valence electrons are rapidly field-ionized and accelerated to MeV energies. These suprathermal electrons further generate fast ions and strong X-ray fluxes in collisional and collision-less processes [163]. The interaction of energetic electrons, ions and photons with the target material results in the production of ions with simple or multiple vacancies in inner atomic shells (also called hollow ions, HI) [164]. The ionization cross-sections due to the impact of positive charged particles are usually small, thus the most effective mechanisms for generation of HI with single or double vacancies in the K-shell of mid-Z elements can be schematically described by a successive atom ionization of the type

$$\mathrm{K}^{2(1)}\mathrm{L}^x\mathrm{M}^y\mathrm{N}^z + \begin{matrix}\mathrm{e}_{\mathrm{hot}}\\ h\nu_{\mathrm{pl}}\end{matrix} \rightarrow \mathrm{K}^{1(0)}\mathrm{L}^x\mathrm{M}^y\mathrm{N}^z + \begin{matrix}2\mathrm{e}\\ \mathrm{e}\end{matrix}, \tag{6}$$

where x, y and z are the numbers of electrons in L, M and N-shells. $\mathrm{e}_{\mathrm{hot}}$ is the interacting hot electron and $h\nu_{\mathrm{pl}}$ the photon emitted by the plasma. The radiative decay of these auto-ionizing intermediate states results in emission of e.g. K_α or K_β radiation

$$\mathrm{K}^1\mathrm{L}^x\mathrm{M}^y\mathrm{N}^z \rightarrow \mathrm{K}^2\mathrm{L}^{x-1(x)}\mathrm{M}^{y(y-1)}\mathrm{N}^z + h\nu_{\alpha(\beta)}(x,y,z). \tag{7}$$

The optically thin spectra of HI are diagnostically very important, as they originate from inner shell transitions which are weakly affected by coupling effects of the plasma environment [165]. Despite their capability of providing information on non-LTE plasmas, hot electron production, and transient, opacity and radiative effects in interaction experiments with PW lasers [166], the theory of HI emission is not fully understood yet. To shed more light on these phenomena, the experiments directed to observation of suprathermal electron induced K_α transitions from open 3d-shell configurations of partially ionized mid-Z elements at near-solid density will be performed. The obtained results will contribute to the validation of alternate atomic structure calculations including configuration interaction effects [164,167]. The feasibility of this research was confirmed by recent experiments at laser intensities of $5 \times 10^{18} - 2 \times 10^{20}$ W/cm^2 [168,169] (see Fig. 36), where the spectrally and spatially resolved X-ray images of the Cu K_α emission demonstrated the variation of the hot electron generation and propagation in a solid Cu target as a function of the laser beam focusing.

An example of application of high-resolution X-ray spectroscopy in investigation of laser–matter interaction is presented in Fig. 37. The laser accelerated ions produced at the Al foil strike the secondary target and collide with Mg atoms, where their interpenetration is observed via spectral emission of hydrogenic Al and He-like Mg ions.

The second type of spectroscopic experiments concerns the investigation of phenomena related to strong electromagnetic fields of the focused laser beam [171] (noted that strengths of the oscillating electric E [V/cm] and magnetic B [G] fields relate to the laser intensity I [W/cm^2] via the approximate formulas $E = 27.4 \times I^{1/2}$ and $B = 0.1 \times I^{1/2}$) or originating from intense particle currents and charge separation effects inside the laser-produced plasma [172]. While thermal and nonthermal electric fields occurring in plasmas are generally studied from the analysis of the Stark-broadened

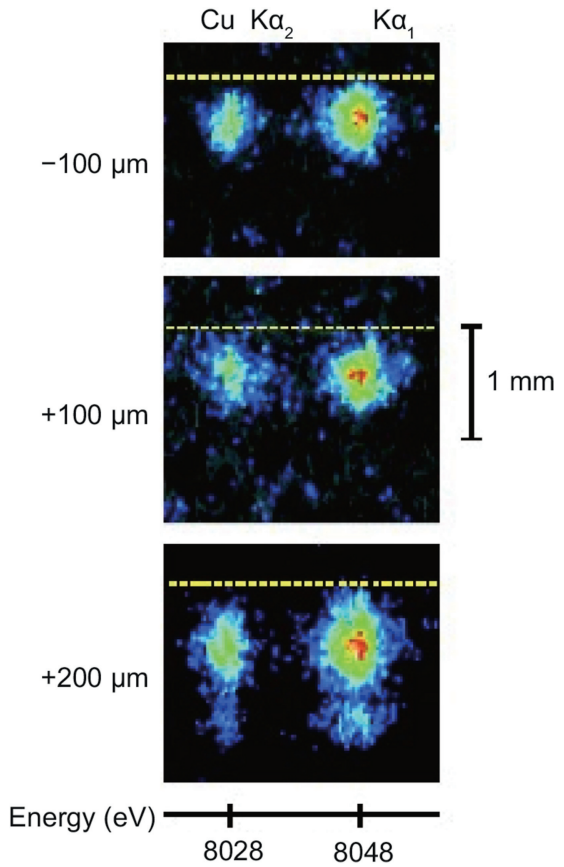

Fig. 36. Hot electron induced Cu K_α emission observed at wedge-shaped massive copper targets. The focusing of the laser beam at variable distances above (negative value) and below (positive values) the target surface (yellow line) affects strongly the interaction conditions and the electron transport [168].

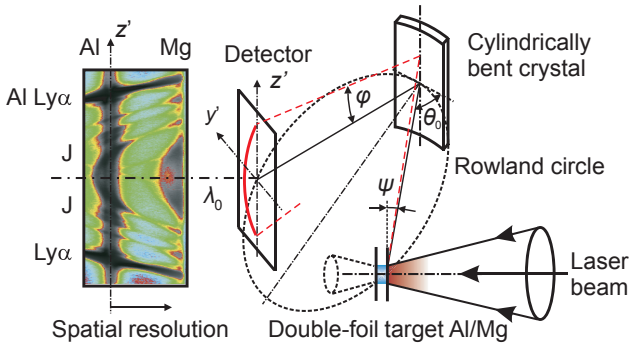

Fig. 37. Plasma formation of a laser-irradiated double-foil Al/Mg target visualized by high resolution X-ray spectroscopy. The laser accelerated Al ions impinge on the Mg foil and interact with counter-streaming Mg ions, the X-ray emission is dispersed using a bent crystal of quartz [170].

profiles of the self-emitted spectral lines, the single-frequency electric fields associated with the collective motion of plasma particles or externally introduced (laser) fields show as local extrema (dips or peaks) in spectral line profiles or of satellite lines close to these transitions (see Ref. [173] and references therein). The effects of magnetic fields are generally much weaker than those of electric fields, thus they are usually neglected. Recently developed models of Stark-Zeeman spectral line shape modification in plasmas [174,175] however indicate that starting from laser intensities 10^{18} W/cm^2, the contributions of magnetic fields cannot be ignored. Consequently the analysis of X-ray self-emission accompanying the laser interaction with mid-Z targets may lead to a development of a new technique for the measurement of laser intensities up to or above 10^{22} W/cm^2. The laser field affected profiles of X-ray spectral lines emitted from the perturbed plasma will be measured using the X-ray spectrometers combining high spectral and spatial resolution and compared with the theoretical predictions. In the first experiments, the high-pressure gas jet targets will be used. The problems with overlapping X-ray emission from field perturbed and non-perturbed plasma will be solved benefiting from polarization properties of otherwise forbidden transitions that become partially allowed in strong field affected plasmas [176]. Alternatively, our experience with identification of electric field affected profiles of spectral lines emitted from independently produced plasmas submitted to external (laser) fields [173] will be used. The obtained results should provide groundwork for the validation of current theoretical models which suffer from a lack of reliable experimental data and, as mentioned above, for development of novel diagnostic techniques.

11. Technology efforts

11.1. Pulsed power device

An external magnetic field has proven to be extremely useful in the study of various laser plasma experiments exploring reconnection [177], astrophysical jets [178], collisionless shocks [40] and even inertial fusion [179,180]. Various approaches have been implemented at different facilties for generating magnetic fields of the order of few tens of Tesla to produce magnetized plasmas. Even the National Ignition Facility (NIF) is currently considering various possibilities for creating external fields [181]. Different technologies have been used at various research facilities for producing such fields – (a) In vacuum coils which implode every shot and produce fields <15 T over a volume of <1 cm^3[179,182], (b) In vacuum Bitter coils which are held with high voltage epoxy and lucite to produce uniform magnetic fields of <13 T over a volume of ≈ 1 cm^3[183], and (c) Re-entrant Helmholtz coil which produce uniform magnetic fields up to 40 T over a volume of ≈ 1 cm^3[64]. While the first option provides an exciting possibility of producing fields with non-trivial structures, the risk of debris damage from the coils is very high. Thus, for magnetized plasma experiments in the P3 chamber, a pulsed power device with parameters similar to Ref. [64] will be implemented. The construction of a ≈ 30 kJ capacitor bank made of 5 capacitors of 54 μF each (part number E59.E53-543010 by Electronicon) is underway. A local and remote control system for the capacitor bank has been developed and tested for energies <10 J. Fig. 38 shows the user interface of the control system. In order to limit the heat dissipated in the Helmholtz coil, the capacitor bank will use thyristor switch (two thyristors in series – part number 5STP 37Y8500 by ABB) instead of ignitrons. Thyristors will ensure that the current flows through the Helmholtz coil only for half a cycle.

11.2. γ-ray detection

Gamma rays in the multi-MeV range have numerous applications in security, medicine and materials science. So far, gamma-rays from high intensity laser–solid interaction have only been generated from Bremsstrahlung emission [184,185]. However, as the focused intensity increases beyond 10^{22} W/cm^2, critical or over dense targets are expected to generate copious amount of gamma-rays because of radiation friction on the accelerated electrons – with the efficiency on conversion as high as 30% for an intensity of 10^{23} W/cm^2 [133,138,139]. This provides the possibility of developing compact gamma-ray sources and is expected to be an important research topic using the 10 PW laser at ELI-Beamlines. Thus the P3 user facility plans to provide several in house

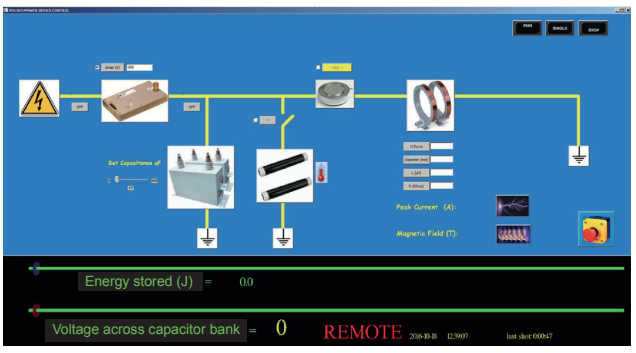

Fig. 38. User interface for the magnetic field power supply.

diagnostics for gamma-ray detection. These include (a) multiple differential filter spectrometers with image plates [186,187], (b) compact bubble detectors (BDS) which use the (γ, n) photonuclear reactions to measure the total flux of γ-rays above thresholds of a few MeV [188], and (c) forward Compton scattering based γ-ray spectrometer. The principle of operation of this third kind of spectrometer is explained in Fig. 39. Compton scattered electrons in the forward direction from a material with low atomic number have their energy proportional to the incoming gamma ray photon. Thus a static magnetic field spectrometer to measure the spectrum of Compton scattered electrons will provide information on the spectrum of the incoming γ-ray photons. A prototype spectrometer was developed at ELI-Beamlines. The design is similar to the spectrometer designed by Ref. [189], but is significantly more compact. The spectrometer was recently calibrated at a bremsstrahlung beamline [190]. It provides an energy coverage of $5-20$ MeV with a resolution of about 2 MeV.

11.3. Betatron diagnostic

Laser wakefield acceleration (LWFA) is a well established technique of electron acceleration using high-intensity femtosecond laser pulses propagating through a gas target [191]. In this technique, the propagating laser pulse drives a strongly non-linear plasma wave. Electrons are accelerated by the electric field of this wave to relativistic energies. The total accelerated charge as well as the energy of the accelerated electrons is strongly dependent on the quality of the focus. As the accelerated electrons transversely oscillate within the plasma wave, they produce a highly collimated (≈ 10 mrad) broadband ultrashort soft X-ray beam with an energy of several keV [191], referred to as *betatron radiation* (see Fig. 40 for the setup). The main advantage of this beam is its ultrashort duration of the order of tens fs and its inherent synhroniziation with the driving laser beam, which makes it an ideal probe beam for time-resolved studies in laser–driven experiments. Possible applications of this X-ray beam include absorption spectroscopy [65], diffraction [141] and Phase Contrast Imaging (PCI) studies [192].

The applications include observation of absorption lines to infer the ionization degree and therefore temperature [65], the XANES measurement to investigate the electronic density of states, and therefore ionic correlation and structure of the matter [193]. The relatively low photon flux and high resolution requirements make single-shot spectroscopic measurement

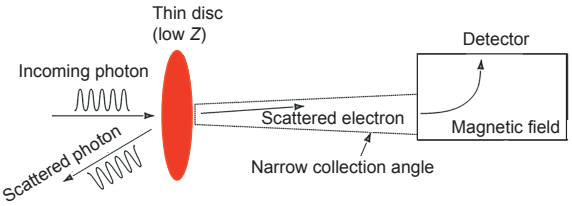

Fig. 39. Schematic of the forward Compton scattering gamma ray spectrometer.

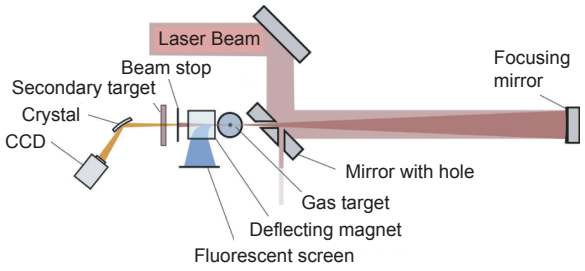

Fig. 40. Schematic setup of the betatron. The beam is directed to the focusing mirror by another mirror with hole allowing on-axis propagation of the focused beam back through it. The beam is focused onto a gas target, where the electron and X-ray beams are generated. The electrons are deflected to a fluoerescent screen within a magnetic spectrometer. The direct X-ray beam penetrates through a secondary target and the resultant absorption spectrum is reflected and dispersed by a diffraction crystal coupled with a CCD.

difficult. To tackle these challenges, an X-ray spectrometer has been developed which uses the cylindrically bent HOPG crystal with high reflectivity and resolution capable of taking a reference on every shot to be used for such applications.

11.4. P3 as a possible EMP test platform

Electromagnetic pulses remain an important research topic [194–196] and are of importance to any petawatt facility [197,198].

Large electro-magnetic pulse (EMP) fields produced during laser matter interaction experiments on high power lasers pose a significant risk to the diagnostics [197,199]. These fields are modeled to be driven by the hot electrons from the target, which excite wave modes corresponding to the resonances of the target chamber. EMP measurements from various short pulse laser facilities have shown the EMP to be linearly proportional to the laser energy. P3 at ELI Beamlines is a large vacuum chamber for experiments with beams with a wide range of parameters: (a) 1 PW with 30 fs duration, (b) 10 PW with 150 fs duration, and (c) ns scale of 1.5 kJ. Thus it provides an exciting prospect for EMP measurements with a variety of beam parameters in the same experimental chamber.

To mitigate the potential effects of EMP at ELI Beamlines, the mesh grid based earthing network was implemented. A welded iron re-bar mesh of about $150\text{mm} \times 150\text{mm}$ was buried in the concrete. Earthing metallic sleeves attached to this grid provide local high frequency grounds in the walls, ceilings and floor of the experimental halls (see Fig. 41). The measured resistance between any two points in the building was less than $0.6\,\Omega$. The doors in the experimental hall provide EMP shielding of at least 50 dB attenuation for electric fields and plane waves from 30 MHz to 20 GHz.

12. High-performance computing and simulation support

12.1. Scientific computing at ELI-Beamlines

Scientific computing is a discipline of great importance in modern research and development. Modern computing power has opened new possibilities for studying and modeling

Fig. 41. Iron re-bar earthing mesh within the concrete walls, floor and ceiling of ELI Beamlines experimental facility. A grounding plate is also shown.

systems with unprecedented levels of detail and this is expected to improve even more in the future. Computational analysis has become a powerful complement to theoretical studies, as it allows us to virtually witness complex phenomena and to test analytical models. We are living in an era in which some computer simulations are so detailed that they are described as *in silico* experiments. This gives an idea of the power of this relatively new field. High Performance Computing, or HPC, is the sub-discipline by which the power of many modern processors is harnessed in a coordinated manner to solve computing problems. Know-how in HPC normally involves the fields of numerical analysis, software engineering, computer hardware, algorithms and field-specific knowledge, as physics, for instance. Strategic development of local HPC know-how is one of the aims at ELI.

ELI's high-power, short time-scale experiments will benefit greatly from modern advances HPC. In fact, for a facility such as this, which involves a large capital investment from public sources, it is essential to maximize its chances of success by the best and most detailed engineering designs and analyses. This is what modern computing allows. From refined models of light propagation, to the interaction of high-power lasers with matter in exotic regimes and more, computational methods will be key tools for gaining insight and predictive power within ELI's research.

ELI recognizes the potential impact of scientific computing on its long term objectives. As a strategy, it plans to benefit from available third-party computing tools while simultaneously fostering in-house capabilities to develop its own solutions to the physics and engineering problems that may arise. ELI's efforts in scientific computing are related with three main areas: development of a Virtual Beamline, development of simulations for experimental design and data analysis, and developing in-house computational science capabilities.

The hardware of the ELI-BL computing cluster ECLIPSE (Extreme Coherent Light Interaction: Plasma Simulations of the Extreme) is summarized in Table 2. In its present size it allows for 2-dimensional kinetic simulations of laser–plasma interaction with Particle-in-Cell codes. Although not that big, it is used by a very small number of people allowing for a very high turnover time for computational runs.

Table 2
Summary of the basic parameters characterizing the ECLIPSE cluster.

Number of computing nodes	84
Total number of cores	1344
Processor type	Haswell-EP (Intel Xeon E5-2630v3)
Node RAM	128 GB (DDR4)
Node hard disk	180 GB
Total RAM	10.75 TB
Peak performance	103 Tflops (single precision)
Network infrastructure	Infiniband non-blocking fat-tree
User data storage (home)	768 TB
Job data storage (scratch)	192 TB

12.2. Start-to-end simulations

Control of laser beam propagation along a beamline and monitoring of beam parameters at any point along a beamline, including at the target location, is an important task for any laser facility. In addition, the study of the laser radiation interaction with matter is essential for ELI Beamlines because of the focus on secondary sources. It is an intriguing aim to have an ability to model all experimental conditions and results before the actual shot. This helps greatly in the design of a real experiment, verification of new ideas and in the understanding of results after experimentation. For instance, the successful operation of a laser wakefiled accelerator depends on many factors including laser pointing stability, pulse front tilt, and laser mode asymmetry. These parameters are in turn dependent on beamline characteristic and laser amplifier output. The solution of this and similar problems requires many simulations, which should be performed in a chain, one by one, forming a start to end simulation.

The numerical analyses described above start with optical simulations. As an example an L3 laser-type system is assumed (1 PW at 30 J, 30 fs at a repetition rate of 10 Hz). The L3 beam is a Super-Gaussian square beam with an edge length of 225.6 mm $(1/e^2)$. The beam runs over 88 m and undergoes up to 18 mirror reflections.

To estimate the beam quality at the end of the beamline, different sources of wavefront distortions have been evaluated along the beamline. For the periscope mirrors, an FEM analyses was performed to rate the impact of the gravity sag and mechanical stress of the frame on the reflected wavefront error. For turning mirrors, given the topography of a real rectangular mirror, 18 random wavefront error profiles were generated such that peak-to-valley and RMS wavefront errors are preserved. The imperfections of L3 compressor gratings were also considered. Phase errors produced by gratings measured under Littrow angle and used as a phase mask for an ideal L3 beam were used for first calculations (see Fig. 42).

The impact of those errors on the beam quality after free space propagation was estimated by means of beam

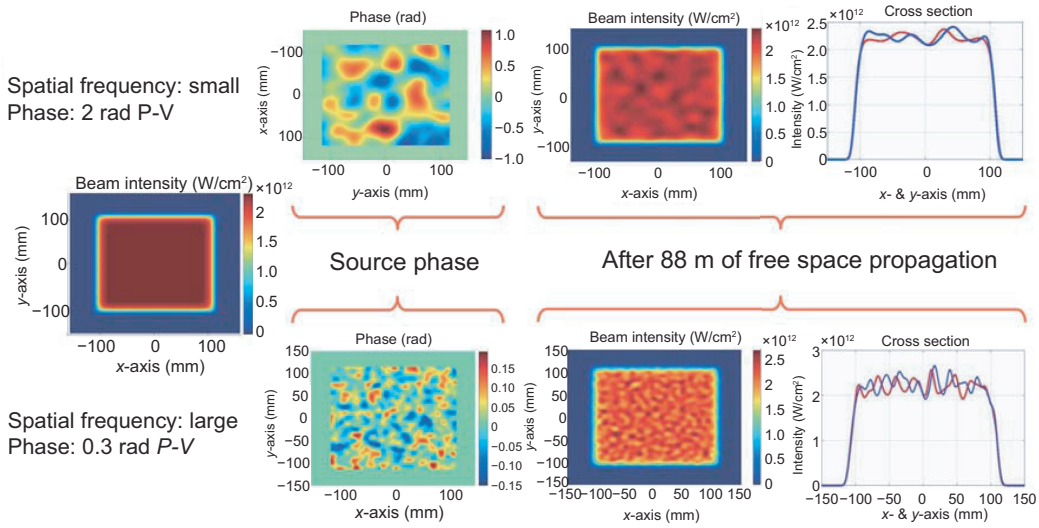

Fig. 42. Examples of phase error propagation in the beam transport system (*P*–*V*: peak to valley variation). The impact of a phase error on the beam profile after free space prorogation. The phase error with a small spatial frequency (upper row) has smaller impact on the beam intensity profile then the phase error with large spatial frequency (lower row) despite the fact that in the latter case the error peak-to-valley value was 6 times lower. The final results need to be compared with real measurements eventually and do also serve as realistic laser input for kinetic simulations of laser–plasma interaction.

propagation calculations. A commercial code, Virtual Lab by LightTrans [200], as well as an in-house developed scalar diffraction propagation code was used. Both codes are benchmarked against each other and found to be in an excellent agreement. Propagation studies show that the compressor grating phase errors has the biggest impact on the beam quality over 88 m. To investigate this part of the beamline in detail, diffraction simulations of the L3 compressor with a 88 nm wide Super-Gaussian spectrum centered at 820 nm need to be pursued.

Using scalar diffraction theory, the far field distribution of the L3 laser beam was calculated while taking into account all the wavefront errors mentioned above. Interfaces to several particle-in-cell plasma codes are available to use a realistic far field distribution for laser–matter interaction simulations. At present work is under way to model numerically in a correct way tight focusing systems where the paraxial approximation is violated.

The ultimate goal is to provide start-to-end simulations including the laser beam propagation, radiation hydrodynamic simulation of plasma generation and expansion due to the laser prepulse, kinetic simulation of the main laser beam interaction with the target and post-processing of energetic particles by Monte-Carlo radiation transport code for shielding and activation simulations.

12.3. Virtual Beamline (VBL)

Future users of the P3 platform as well as of all other experimental stations at ELI Beamlines will be able to benefit from the Virtual Beamline (VBL) – a complex interactive 3D web application that combines detailed models of the facility and equipment with physics simulations and experimental data. The main objective is to provide an integrated tool that helps users to design, configure, simulate, and visualize proposed experiments. Furthermore, the application will also allow access to layouts and datasets for already conducted campaigns. Although the majority of users will likely use standard onscreen way to work with the VBL, during past two years we have developed and tested prototypes of the VBL for virtual reality head-mounted displays. While it is very challenging to process and optimize many extremely detailed CAD models as well as large simulation datasets for real-time interactive visualization, our current applications run at sufficient framerates, which are necessary for immersive experiences. Apart from complete virtual model of the facility and equipment, we have recently developed prototypes that integrate animated 3D PIC simulations for laser–target interaction and Monte Carlo simulations of secondary sources. The main next steps in development of the VBL will be focused on providing features

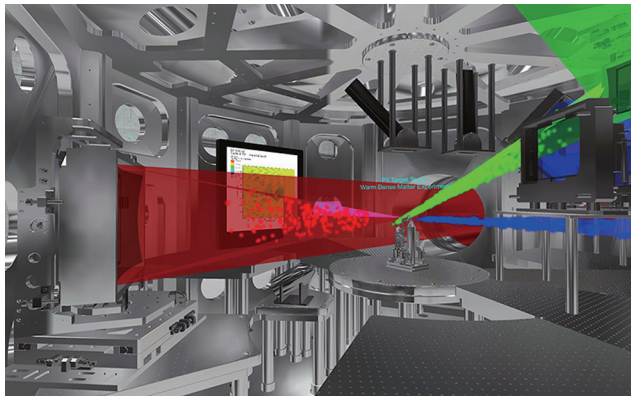

Fig. 43. Screenshot of the P3 chamber interior from the VBL application. The VBL system will allow the user to design online the experimental setup and optimize the layout.

for building experimental layouts through interactive manipulation of individual components and implementation of simulation capabilities through integration with the ECLIPSE HPC cluster (Fig. 43).

13. Conclusion and outlook

The P3 installation of ELI-Beamlines will be a unique platform for research on any topic related to high-energy-density physics and ultra-high intensity interaction. It will be a multi-functional user facility open to the international community. P3 will allow to combine high-energy and high-intensity laser–plasma interaction in a flexible way. Although the construction is challenging, the potential benefit for the user community will be tremendous.

The present ELI pillars can also serve as a testing ground for the future fourth pillar of ELI, dedicated to high-field research only, and which will provide laser powers above 100 PW.

Acknowledgements

The authors acknowledge support from the project ELI: Extreme Light Infrastructure from European Regional Development (CZ.02.1.01/0.0/0.0/15-008/0000162). Also supported by the project High Field Initiative (CZ.02.1.01/0.0/0.0/15-003/0000449) from European Regional Development Fund.

References

[1] D. Strickland, G. Mourou, Compression of amplified chirped optical pulses, Opt. Comm. 56 (1985) 219.
[2] G. Mourou, C. Barty, M. Perry, Ultrahigh-intensity lasers: physics of the extreme on a tabletop, Phys. Today 51 (1998) 22.
[3] A. Dubietis, G. Jonusauskas, A. Piskarskas, Powerful femtosecond pulse generation by chirped and stretched pulse parametric amplification in BBO crystal, Opt. Comm. 88 (1992) 437.
[4] Extreme Light Infrastructure: http://www.eli-laser.eu.
[5] B. LeGarrec, S. Sebban, D. Margarone, M. Precek, S. Weber, et al., Eli-beamlines: extreme light infrastructure science and technology with ultra-intense lasers, Proc. SPIE 8962 (2014) 8962OI.
[6] B. Rus, P. Bakule, D. Kramer, J. Naylon, J. Thoma, et al., Eli-beamlines: development of next generation short-pulse laser systems, Proc. SPIE 9515 (2015) 9515OF.
[7] Extreme Light Infrastructure Beamlines: http://www.eli-beams.eu.
[8] G. Mourou, G. Korn, W. Sandner, J. Collier (Eds.), ELI Extreme Light Infrastructure (Whitebook), THOSS Media GmbH, Berlin, Germany, 2011.
[9] S.V. Lebedev (Ed.), High Energy Density Laboratory Astrophysics, Springer Verlag Berlin, Germany, 2007.
[10] S. Bulanov, T. Esirkepov, M. Kando, J. Koga, K. Kondo, et al., On the problems of relativistic laboratory astrophysics and fundamental physics with super powerful lasers, Plasma Phys. Rep. 41 (2015) 1.
[11] D. Ryutov, R. Drake, B. Remington, Criteria for scaled laboratory simulations of astrophysical MHD phenomena, Astrophys. J. 127 (2000) 465.
[12] B. Remington, D. Arnett, R. Drake, H. Takabe, Modeling astrophysics phenomena in the laboratory with intense lasers, Science 284 (1999) 1488.
[13] C. Li, P. Tzeferacos, D. Lamb, G. Gregori, P. Norreys, et al., Scaled laboratory experiments explain the kink behaviour of the Crab Nebula jet, Nat. Comm. 7 (2016) 13081.
[14] M. Marklund, P. Shukla, Nonlinear collective effects in photon-photon and photon-plasma interactions, Rev. Mod. Phys. 78 (2006) 591.
[15] G. Mourou, T. Tajima, S. Bulanov, Optics in the relativistic regime, Rev. Mod. Phys. 78 (2006) 309.
[16] Y. Salamin, S. Hu, K. Hatsagortsyan, C. Keitel, Relativistic high-power laser-matter interaction, Phys. Rep. 427 (2006) 41.
[17] T. Brabec (Ed.), Strong Field Laser Physics, Springer Verlag, 2008.
[18] A. DiPiazza, C. Müller, K.Z. Hatsagortsyan, C.H. Keitel, Extremely high-intensity laser interactions with fundamental quantum systems, Rev. Mod. Phys. 84 (2012) 1177.
[19] DOE Office of Science and National Nuclear Security Administration, Basic Research Needs for High Energy Density Density Laboratory Physics, US Department of Energy, 2009.
[20] R. Drake, High-energy-density-physics: Fundamentals, Inertial Fusion, and Experimental Astrophysics, Springer Verlag Berlin, Germany, 2006.
[21] F. Graziani, M. Desjarlais, R. Redmer, S. Trickey (Eds.), Frontiers and Challenges in Warm Dense Matter, Springer International Publishing, Berlin, Germany, 2014.
[22] R. Kirkwood, J. Moody, J. Kline, E. Dewald, S. Glenzer, et al., A review of laser-plasma interaction physics of indirect-drive fusion,, Plasma. Phys. control. Fusion 55 (2013) 103001.
[23] S. Weber, C. Riconda, Temperature dependence of parametric instabilities in the context of the shock-ignition approach to inertial confinement fusion, High. Power Laser Sci. Eng. 3 (2015) e6.
[24] C. Riconda, S. Weber, Raman-Brillouin interplay for inertial confinement fusion relevant laser-plasma interaction, High. Power Laser Sci. Eng. 4 (2016) e23.
[25] J. Fuchs, A. Gonoskov, M. Nakatsutsumi, W. Nazarov, F. Quéré, et al., Plasma devices for focusing extreme light pulses, Eur. Phys. J. Spec. Top. 223 (2014) 1169.
[26] G. Lehmann, K. Spatschek, Transient plasma photonic crystals for high-power lasers, Phys. Rev. Lett. 116 (2016) 225002.
[27] B. Gonzalez-Izquierdo, R. Gray, M. King, R. Dance, R. Wilson, et al., Optically controlled dense current structures driven by relativistic plasma aperture-induced diffraction, Nat. Phys. 12 (2016) 505.
[28] R. Clarke, S. Dorkings, R. Heathcote, K. Markey, D. Neely, Proton activation history on the vulcan high-intensity petawatt laser facility, Laser Part. Beams 32 (2014) 455.
[29] T. Bohlen, F. Cerutti, M. Chin, A. Fassò, A. Ferrari, et al., The fluka code: developments and challenges for high energy and medical applications, Nucl. Data Sheets 120 (2014) 211.
[30] A. Ferrari, P. Sala, A. Fassò, J. Ranft, Fluka: a multi-particle transport code, Tech. Rep., CERN-2005-10, 2005. INFN/TC_05/11, SLAC-R-773(2005).
[31] V. Vlachoudis, Flair: A Powerful but User Friendly Graphical Interface for Fluka, Tech. rep., Proc. Int. Conf. on Mathematics, Computational Methods & Reactor Physics (M&C 2009), vol. 2009, Saratoga Springs, New York, 2009. URL, http://www.fluka.org/flair/Flair_MC2009.pdf.
[32] Protection of the public in situations of prolonged radiation exposure, Tech. Rep., ICRP Publication 82, Ann. ICRP 29 (1–2) (1999).
[33] Czech Republic Decree No. 307/2002 Coll. On Radiation Protection.
[34] F. Sylla, M. Veltcheva, S. Kahaly, A. Flacco, V. Malka, Development and characterization of very dense submillimetric gas jets for laser-plasma interaction, Rev. Sci. Instrum. 83 (2012) 033507.
[35] S. Garcia, D. Chatain, J. Perin, Continuous production of a thin ribbon of solid hydrogen, Laser Part. Beams 32 (2014) 569.
[36] D. Ryutov, R.P. Drake, J. Kane, E. Liang, B.A. Remington, et al., Similarity criteria for the laboratory simulation of supernova hydrodynamics, Astrophys. J. 518 (1999) 821.
[37] D.D. Ryutov, B.A. Remington, H.F. Robey, R.P. Drake, Magnetohydrodynamic scaling: from astrophysics to the laboratory, Phys. Plasmas 8 (2001) 1804.
[38] D. Ryutov, N. Kugland, H. Park, C. Plechaty, B. Remington, et al., Basic scalings for collisionless-shock experiments in a plasma without pre-imposed magnetic field, Plasma Phys. Control. Fusion 54 (2012) 105021.

[39] P.M. Nilson, L. Willingale, M.C. Kaluza, C. Kamperidis, S. Minardi, et al., Phys. Rev. Lett. 97 (2006) 255001.
[40] W. Fox, G. Fiksel, A. Bhattacharjee, P.-Y. Chang, K. Germaschewski, et al., Filamentation instability of counterstreaming laser-driven plasmas, Phys. Rev. Lett. 111 (2013) 225002.
[41] C.K. Li, D.D. Ryutov, S.X. Hu, M.J. Rosenberg, A.B. Zylstra, et al., Structure and dynamics of colliding plasma jets, Phys. Rev. Lett. 111 (2013) 235003.
[42] E.C. Harding, J.F. Hansen, O.A. Hurricane, R.P. Drake, H.F. Robey, et al., Observation of a kelvin-helmholtz instability in a high-energy-density plasma on the omega laser, Phys. Rev. Lett. 103 (2009) 045005.
[43] J. Yoo, M. Yamada, H. Ji, C. Myers, Observation of ion acceleration and heating during collisionless magnetic reconnection in a laboratory plasma, Phys. Rev. Lett. 110 (2013) 215007.
[44] Y. Gu, O. Klimo, D. Kumar, Y. Liu, S. Singh, et al., Fast magnetic-field annihilation in the relativistic collisionless regime driven by two ultrashort high-intensity laser pulses, Phys. Rev. E 93 (2016) 013203.
[45] Y. Gu, Q. Yu, O. Klimo, T. Esirkepov, S. Bulanov, et al., Fast magnetic energy dissipation in relativistic plasma induced by high order laser modes, High. Power Laser Sci. Eng. 4 (2016) e19.
[46] Y. Gu, O. Klimo, D. Kumar, S. Bulanov, T. Esirkepov, et al., Fast magnetic field annihilation driven by two laser pulses in underdense plasma, Phys. Plasmas 22 (2015) 103113.
[47] J. Workman, J.R. Fincke, P. Keiter, G.A. Kyrala, Development of intense point x-ray sources for backlighting high energy density experiments, Rev. Sci. Instrum. 3915 (2004).
[48] H.-S. Park, D.M. Chambers, H.-K. Chung, R.J. Clarke, R. Eagleton, et al., High-energy ka radiography using high-intensity, short-pulse lasers, Phys. Plasmas 13 (2006) 056309.
[49] A. Ovchinnikov, O. Kostenko, O. Chefonov, O. Rosmej, N. Andreev, et al., Characteristic x-rays generation under the action of femtosecond laser pulses on nano-structured targets, Laser Part. Beams 29 (2011) 249.
[50] M.A. Purvis, V.N. Shlyaptsev, R. Hollinger, C. Bargsten, A. Pukhov, et al., Relativistic plasma nanophotonics for ultrahigh energy density physics, Nat. Photonics 7 (2013) 796.
[51] S. Glenzer, R. Redmer, X-ray thomson scattering in high energy density plasmas, Rev. Mod. Phys. 81 (2009) 1625.
[52] P.K. Patel, A.J. Mackinnon, M.H. Key, T.E. Cowan, M.E. Foord, et al., Isochoric heating of solid-density matter with an ultrafast proton beam, Phys. Rev. Lett. 91 (2003) 125004.
[53] S. Mangles, C.D. Murphy, Z. Najmudin, A. Thomas, Monoenergetic beams of relativistic electrons from intense laser-plasma interactions, Nature (2004).
[54] C.G.R. Geddes, K. Nakamura, G.R. Plateau, C. Toth, E. Cormier-Michel, et al., Plasma-density-gradient injection of low absolute-momentum-spread electron bunches, Phys. Rev. Lett. 100 (2008) 215004.
[55] Z.-H. He, A.G.R. Thomas, B. Beaurepaire, J.A. Nees, B. Hou, et al., Electron diffraction using ultrafast electron bunches from a laser-wakefield accelerator at khz repetition rate, Appl. Phys. Lett. 102 (2013).
[56] H. Habara, K. Ohta, K.A. Tanaka, G.R. Kumar, M. Krishnamurthy, et al., Direct, absolute, and *in Situ* measurement of fast electron transport via cherenkov emission, Phys. Rev. Lett. 104 (2010) 055001.
[57] M. Roth, D. Jung, K. Falk, N. Guler, O. Deppert, et al., Bright laser-driven neutron source based on the relativistic transparency of solids, Phys. Rev. Lett. 110 (2013) 044802.
[58] N. Guler, P. Volegov, A. Favalli, F.E. Merrill, K. Falk, et al., Neutron imaging with the short-pulse laser driven neutron source at the trident laser facility, J. Appl. Phys. 120 (2016) 154901.
[59] T. Guillot, Interiors of giant planets inside and outside the solar system, Science 286 (5437) (1999) 72.
[60] Nuckolls, Laser compression of matter to super-high densities: thermonuclear (CTR) applications, Nature 239 (1972) 139.
[61] R.L. McCrory, D.D. Meyerhofer, S.J. Loucks, S. Skupsky, R. Betti, et al., Progress in direct-drive inertial confinement fusion research at the laboratory for laser energetics, Eur. Phys. J. D. 44 (2007) 233.
[62] K.P. Driver, B. Militzer, All-electron path integral monte carlo simulations of warm dense matter: application to water and carbon plasmas, Phys. Rev. Lett. 108 (2012) 115502.
[63] D. Saumon, C. Starrett, J. Kress, J. Clérouin, The quantum hypernetted chain model of warm dense matter, High. Energy Density Phys. 8 (2012) 150.
[64] B. Albertazzi, B. Béard, A. Ciardi, T. Vinci, J. Albrecht, et al., Production of large volume, strongly magnetized laser-produced plasmas by use of pulsed external magnetic fields, Rev. Sci. Instrum. 84 (2013) 043505.
[65] M.Z. Mo, Z. Chen, S. Fourmaux, A. Saraf, K. Otani, et al., Laser wakefield generated x-ray probe for femtosecond time-resolved measurements of ionization states of warm dense aluminum, Rev. Sci. Instrum. 84 (2013) 123106.
[66] R.F. Smith, J.H. Eggert, M.D. Saculla, A.F. Jankowski, M. Bastea, et al., Ultrafast dynamic compression technique to study the kinetics of phase transformations in bismuth, Phys. Rev. Lett. 101 (2008) 065701.
[67] D.G. Hicks, T.R. Boehly, P.M. Celliers, J.H. Eggert, S.J. Moon, et al., Laser-driven single shock compression of fluid deuterium from 45 to 220 gpa, Phys. Rev. B 79 (2009) 014112.
[68] K. Falk, C.A. McCoy, C.L. Fryer, C.W. Greeff, A.L. Hungerford, et al., Temperature measurements of shocked silica aerogel foam, Phys. Rev. E 90 (2014) 033107.
[69] K. Falk, E.J. Gamboa, G. Kagan, D.S. Montgomery, B. Srinivasan, et al., Equation of state measurements of warm dense carbon using laser-driven shock and release technique, Phys. Rev. Lett. 112 (2014) 155003.
[70] S.H. Glenzer, G. Gregori, R.W. Lee, F.J. Rogers, S.W. Pollaine, et al., Demonstration of spectrally resolved x-ray scattering in dense plasmas, Phys. Rev. Lett. 90 (2003) 175002.
[71] P.M. Celliers, D.K. Bradley, G.W. Collins, D.G. Hicks, T.R. Boehly, et al., Line-imaging velocimeter for shock diagnostics at the OMEGA laser facility, Rev. Sci. Instrum. 75 (2004) 4916.
[72] M.C. Gregor, R. Boni, A. Sorce, J. Kendrick, C.A. McCoy, et al., Absolute calibration of the OMEGA streaked optical pyrometer for temperature measurements of compressed materials. Rev. Sci. Instrum. 87 (2016) 114903.
[73] D. Kraus, A. Ravasio, M. Gauthier, D.O. Gericke, Nanosecond formation of diamond and lonsdaleite by shock compression of graphite, Nature 10970 (2016).
[74] P. McKenna, A.P.L. Robinson, D. Neely, M.P. Desjarlais, D.C. Carroll, et al., Effect of lattice structure on energetic electron transport in solids irradiated by ultraintense laser pulses, Phys. Rev. Lett. 106 (2011) 185004.
[75] A. Schropp, R. Hoppe, V. Meier, J. Patommel, F. Seiboth, et al., Imaging shock waves in diamond with both high temporal and spatial resolution at an XFEL. Sci. Rep. 5 (2015) 11089.
[76] G. Gregori, S.H. Glenzer, W. Rozmus, R.W. Lee, O.L. Landen, Theoretical model of x-ray scattering as a dense matter probe, Phys. Rev. E 67 (2003) 026412.
[77] S. Atzeni, J. Meyer-ter-Vehn, The Physic of Inertial Fusion, Clarendon Press, Oxford, United Kingdom, 2004.
[78] O. Hurricane, D. Callahan, D. Casey, P. Celliers, C. Cerjan, et al., Fuel gain exceeding unityin an inertially confined fusion implosion, Nature 506 (2014) 343.
[79] R. Betti, O. Hurricane, Inertial-confinement fusion with lasers, Nat. Phys. 12 (2016) 435.
[80] R. Betti, C. Zhou, K. Anderson, L. Perkins, W. Theobald, et al., Shock ignition of thermonuclear fuel with high areal density, Phys. Rev. Lett. 98 (2007) 155001.
[81] S. Atzeni, X. Ribeyre, G. Schurtz, A. Schmitt, B. Canaud, et al., Shock ignition of thermonuclear fuels: principles and modelling, Nucl. Fusion 54 (2014) 054008.
[82] D. Batani, S. Baton, A. Casner, S. Depierreux, M. Hohenberger, et al., Physics issues for shock ignition, Nucl. Fusion 54 (2014) 054009.
[83] D. Batani, L. Antonelli, G. Folpini, Y. Maheut, L. Giuffrida, et al., Generation of high pressure shocks relevant to the shock-ignition intensity regime, Phys. Plasmas 21 (2014) 032710.

[84] V. Tikhonchuk, A. Colaitis, A. Vallet, E. Llor Aisa, G. Duchateau, et al., Physics of laser-plasma interaction for shock ignition of fusion reactions, Plasma Phys. control. Fusion 58 (2015) 014018.
[85] G. von Guderley, Starke kugelige und zylindrische Verdichtungsstösse in der Nähe des Kugelmittelpunktes bzw. der Zylinderachse, Luftfahrt-Forsch 9 (1942) 302.
[86] K. Brueckner, S. Jorna, Laser-driven fusion, Rev. Mod. Phys. 46 (1974) 325.
[87] V. Shcherbakov, Ignition of a laser-fusion target by a focusing shock wave, Sov. J. Plasma Phys. 9 (1983) 240.
[88] X. Ribeyre, G. Schurtz, M. Lafon, S. Galera, S. Weber, Shock ignition: an alternative scheme for HiPER, Plasma Phys. control. Fusion 51 (2009) 015013.
[89] X. Ribeyre, M. Lafon, G. Schurtz, M. Olazabal-Loumé, J. Breil, et al., Shock ignition: modelling and target design robustness, Plasma Phys. control. Fusion 51 (2009) 124030.
[90] O. Klimo, S. Weber, V. Tikhonchuk, J. Limpouch, Particle-in-cell simulations of laser-plasma interaction for the shock ignition scenario, Plasma. Phys. Control. Fusion 52 (2010) 055013.
[91] O. Klimo, J. Psikal, V. Tikhonchuk, S. Weber, Two-dimensional simulations of laser-plasma interaction and hot electron generation in the context of shock-ignition research, Plasma. Phys. Control. Fusion 56 (2014) 055010.
[92] C. Riconda, S. Weber, V. Tikhonchuk, A. Heron, Kinetic simulations of stimulated Raman backscattering and related processes for the shock-ignition approach to inertial confinement fusion, Phys. Plasmas 18 (2011) 092701.
[93] S. Weber, C. Riconda, O. Klimo, A. Heron, V. Tikhonchuk, Fast saturation of the two-plasmon-decay instability for shock-ignition conditions, Phys. Rev. E 85 (2012) 016403.
[94] M. Temporal, B. Canaud, W. Garbett, R. Ramis, S. Weber, Irradiation uniformity at the laser magajoule facility in the context of the shock ignition scheme, High. Power Laser Sci. Eng. 2 (2014) e8.
[95] S. Weber, G. Riazuelo, P. Michel, R. Loubere, F. Walraet, et al., Modeling of laser-plasma interaction on hydrodynamic scales: physics development and comparison with experiments, Laser Part. Beams 22 (2004) 189.
[96] S. Weber, P. Maire, R. Loubere, G. Riazuelo, P. Michel, et al., Modeling of laser-plasma interaction on hydrodynamic scales: physics development and comparison with experiments, Comp. Phys. Comm. 168 (2005) 141.
[97] M. Holec, J. Limpouch, R. Liska, S. Weber, High-order discontinuous galerkin nonlocal transport and energy equations scheme for radiation hydrodynamics, Int. J. Numer. Meth. Fluids 83 (2017) 779, http://dx.doi.org/10.1002/fld.4288.
[98] L.L. Ji, J. Snyder, A. Pukhov, R.R. Freeman, K.U. Aklib, Towards manipulating relativistic laser pulses with micro-tube plasma lenses, Sci. Rep. 6 (2016) 23256.
[99] S. Monchocé, S. Kahaly, A. Leblanc, L. Videau, P. Combis, et al., Optically controlled solid-density transient plasma gratings, Phys. Rev. Lett. 112 (2014) 145008.
[100] G. Scott, V. Bagnoud, C. Brabetz, R. Clarke, J. Green, et al., Optimization of plasma mirror reflectivity and optical quality using double laser pulses, New J. Phys. 17 (2015) 033027.
[101] M. Maier, W. Kaiser, J. Giordmaine, Intense light bursts in the stimulated Raman effect, Phys. Rev. Lett. 17 (1966) 1275.
[102] R. Milroy, C. Capjack, C. James, A plasma-laser amplifier in the 11−16μm wavelength range, Plasma Phys. 19 (1977) 989.
[103] R. Milroy, C. Capjack, C. James, Plasma laser pulse amplifier using induced raman or brillouin processes, Phys. Fluids 22 (1979) 1922.
[104] C. Capjack, C. James, J. McMullin, Plasma krf laser pulse compressor, J. Appl. Phys. 53 (1982) 4046.
[105] A. Andreev, A. Sutyagin, Feasibility of optical pulse compression by stimulated brillouin scattering in a plasma, Sov. J. Quantum Electron 19 (1989) 1579.
[106] Z. Sheng, J. Zhang, D. Umstadter, Femtosecond laser induced plasma diffraction gratings in air as photonic devices for high intensity laser applications, Appl. Phys. 77 (2003) 673.
[107] D. Forslund, J. Kindel, E. Lindman, Theory of stimulated scattering processes in laser-irradiated plasmas, Phys. Fluids 18 (1975) 1002.
[108] D. Ristau (Ed.), Laser-induced Damage in Optical Materials, Taylor and Francis Inc, 2014.
[109] A. Andreev, C. Riconda, V. Tikhonchuk, S. Weber, Short light pulse amplification and compression by stimulated brillouin scattering in plasmas in the strong coupling regime, Phys. Plasmas 13 (2006) 053110.
[110] S. Weber, C. Riconda, L. Lancia, J.-R. Marquès, G. Mourou, et al., Amplification of ultrashort laser pulses by Brillouin backscattering in plasmas, Phys. Rev. Lett. 111 (2013) 055004.
[111] A. Frank, J. Fuchs, L. Lehmann, J.-R. Marquès, G. Mourou, et al., Amplification of ultra-short light pulses by ion collective modes in plasmas, Eur. Phys. J. Spec. Top. 223 (2014) 1153.
[112] C. Riconda, S. Weber, L. Lancia, J.-R. Marquès, G. Mourou, et al., Spectral characteristics of ultra-hort laser pulses in plasma amplifiers, Phys. Plasmas 20 (2013) 083115.
[113] C. Riconda, S. Weber, L. Lancia, J.-R. Marquès, G. Mourou, et al., Plasma-based creation of short light pulses: analysis and simulation of amplification and focusing, Plasma Phys. control. Fusion 57 (2015) 014002.
[114] M. Chiaramello, C. Riconda, F. Amiranoff, J. Fuchs, M. Grech, et al., Optimization of interaction conditions for efficient short laser pulse amplification by stimulated brillouin scattering in the strongly coupled regime, Phys. Plasmas 23 (2016) 072103.
[115] M. Chiaramello, F. Amiranoff, C. Riconda, S. Weber, Role of frequency chirp and energy flow directionality in the strong coupling regime of brillouin-based plasma amplification, Phys. Rev. Lett. 117 (2016) 235003.
[116] G. Lehmann, F. Schluck, K. Spatschek, Regions for brillouin seed pulse growth in relativistic laser-plasma interaction, Phys. Plasmas 19 (2012) 093120.
[117] G. Lehmann, K. Spatschek, Nonlinear brillouin amplification of finite-duration seeds in the strong coupling regime, Phys. Plasmas 20 (2016) 073112.
[118] G. Lehmann, K. Spatschek, Temperature dependence of seed pulse amplitude and density grating in brillouin amplification, Phys. Plasmas 23 (2016) 023107.
[119] F. Schluck, G. Lehmann, K. Spatschek, Amplification of a seed pumped by a chirped laser in the strong coupling brillouin regime, Phys. Plasmas 22 (2015) 093104.
[120] F. Schluck, G. Lehmann, C. Müllwer, K. Spatschek, Dynamical transition between weak and strong coupling in brillouin laser pulse amplification, Phys. Plasmas 23 (2016) 083105.
[121] L. Lancia, J.-R. Marquès, M. Nakatsutsumi, C. Riconda, S. Weber, et al., Experimental evidence of short light pulse amplification using strong-coupling stimulated Brillouin scattering in the pump depletion regime, Phys. Rev. Lett. 104 (2010) 025001.
[122] L. Lancia, A. Giribono, L. Vassura, M. Chiaramello, C. Riconda, et al., Signatures of the self-similar regime of strongly coupled stimulated Brillouin scattering for efficient short laser pulse amplification, Phys. Rev. Lett. 116 (2016) 075001.
[123] S. Bahk, P. Rousseau, T. Planchon, V. Chvykov, G. Kalintchenko, et al., Generation and characterization of the highest laser intensities (10^{22}W/cm^2), Opt. Lett. 29 (2004) 2837.
[124] A. Kon, M. Nakatsutsumi, S. Buffechoux, Z.L. Chen, J. Fuchs, et al., Geometrical optimization of an ellipsoidal plasma mirror toward tight focusing of ultra-intense laser pulse, J. Phys. Conf. Ser. 244 (2010) 032008.
[125] M. Nakatsutsumi, A. Kon, S. Buffechoux, P. Audebert, J. Fuchs, et al., Fast focusing of short-pulse lasers by innovative plasma optics toward extreme intensity, Opt. Lett. 35 (2010) 2314.
[126] M. Nakatsutsumi, Y. Sentoku, S. N. Chen, S. Buffechoux, A. Kon, et al., On magnetic inhibition of laser-driven, sheath-accelerated high-energy protons (Submitted for publication).
[127] R. Wilson, M. King, R.J. Gray, D.C. Carroll, R.J. Dance, et al., Ellipsoidal plasma mirror focusing of high power laser pulses to ultra-high intensities, Phys. Plasmas 23 (2016) 033106.

[128] T.-M. Jeong, S. Weber, B. LeGarrec, D. Margarone, T. Mocek, et al., Spatio-temporal modification of femtosecond focal spot under tight focusing condition, Opt. Express 23 (2015) 11641.
[129] I. Thiele, S. Skupin, R. Nuter, Boundary conditions for arbitrarily shaped and tightly focused laser pulses in electromagnetic codes, J. Comput. Phys. 321 (2016) 1110.
[130] V. Ritus, Quantum effects of the interaction of elementary particles with an intense electromagnetic field, J. Sov. Laser Res. 6 (1985) 497.
[131] S. Bulanov, T. Esirkepov, Y. Hayashi, M. Kando, H. Kiriyama, et al., On the design of experiments for the study of extreme field limits in the interaction of laser with ultrarelativistic electron beam, Nucl. Instrum. Methods Phys. Research Sec. A: accelerators, Spectrometers, Detect. Assoc. Equip. 660 (2011) 31.
[132] G. Lowenthal, P. Airey, Practical Applications of Radioactivity and Nuclear Radiations: An Introductory Text for Engineers, Scientists, Teachers, and Students, Cambridge University Press, Cambridge ; New York, 2001.
[133] T. Nakamura, J. Koga, T. Esirkepov, M. Kando, G. Korn, et al., High-power γ-ray flash generation in ultraintense laser-plasma interaction, Phys. Rev. Lett. 108 (2012) 195001.
[134] D. Thompson, Highlights of GeV gamma-ray astronomy, Astrophys. Space Sci. Trans. 6 (2010) 59.
[135] J. Wardle, D. Homan, R. Ojha, D. Roberts, Electron-positron jets associated with the quasar 3c279, Nature 395 (1998) 457.
[136] F.A. Aharonian, A.G. Akhperjanian, K.-M. Aye, A.R. Bazer-Bachi, M. Beilicke, et al., High-energy particle acceleration in the shell of a supernova remnant, Nature 432 (2004) 75.
[137] Y. Lau, F. He, D. Umstadter, R. Kowalczyk, Nonlinear Thomson scattering: a tutorial,, Phys. Plasmas 10 (2003) 2155.
[138] R. Capdessus, E. d'Humières, V.T. Tikhonchuk, Influence of ion mass on laser-energy absorption and synchrotron radiation at ultrahigh laser intensities, Phys. Rev. Lett. 110 (2013) 215003.
[139] D.J. Stark, T. Toncian, A.V. Arefiev, Enhanced multi-mev photon emission by a laser-driven electron beam in a self-generated magnetic field, Phys. Rev. Lett. 116 (2016) 185003.
[140] K. Ta Phuoc, S. Corde, C. Thaury, V. Malka, A. Tafzi, et al., All-optical compton gamma-ray source, Nat. Phot. 6 (2012) 308.
[141] L.M. Chen, W.C. Yan, D.Z. Li, Z.D. Hu, L. Zhang, et al., Bright betatron x-ray radiation from a laser-driven-clustering gas target, Sci. Rep. 3 (2013) 1912.
[142] N.D. Powers, I. Ghebregziabher, G. Golovin, C. Liu, S. Chen, et al., Quasi-monoenergetic and tunable x-rays from a laser-driven compton light source, Nat. Phot. 8 (2014) 28.
[143] G. Sarri, D.J. Corvan, W. Schumaker, J.M. Cole, A. Di Piazza, et al., Ultrahigh brilliance multi-mev γ-ray beams from nonlinear relativistic thomson scattering, Phys. Rev. Lett. 113 (2014) 224801.
[144] K. Khrennikov, J. Wenz, A. Buck, J. Xu, M. Heigoldt, et al., Tunable all-optical quasimonochromatic thomson x-ray source in the nonlinear regime, Phys. Rev. Lett. 114 (2015) 195003.
[145] A.G.R. Thomas, C.P. Ridgers, S.S. Bulanov, B.J. Griffin, S.P.D. Mangles, Strong radiation-damping effects in a gamma-ray source generated by the interaction of a high-intensity laser with a wakefield-accelerated electron beam, Phys. Rev. X 2 (2012) 041004.
[146] M. Vranic, J.L. Martins, J. Vieira, R.A. Fonseca, L.O. Silva, All-optical radiation reaction at $10^{21}\mathrm{W/cm}^2$, Phys. Rev. Lett. 113 (2014) 134801.
[147] J. Schwinger, On gauge invariance and vacuum polarization, Phys. Rev. 82 (1951) 664.
[148] N. Neitz, A. Di Piazza, Stochasticity effects in quantum radiation reaction, Phys. Rev. Lett. 111 (2013) 054802.
[149] T.G. Blackburn, C.P. Ridgers, J.G. Kirk, A.R. Bell, Quantum radiation reaction in laser-electron-beam collisions, Phys. Rev. Lett. 112 (2014) 015001.
[150] S.R. Yoffe, Y. Kravets, A. Noble, D.A. Jaroszynski, Longitudinal and transverse cooling of relativistic electron beams in intense laser pulses, New J. Phys. 17 (2015) 053025.
[151] M. Vranic, T. Grismayer, R.A. Fonseca, L.O. Silva, Quantum radiation reaction in head-on laser-electron beam interaction, New J. Phys. 18 (2016) 073035.
[152] Y. Gu, O. Klimo, S. Weber, G. Korn, High density ultrashort relativistic positron beam generation by laser-plasma interaction, New J. Phys. 18 (2016) 113023.
[153] S. Bulanov, C. Schroeder, E. Esarey, W. Leemans, Electromagnetic cascade in high-energy electron, positron, and photon interactions with intense laser pulses, Phys. Rev. A 87 (2013).
[154] G. Breit, J.A. Wheeler, Collision of two light quanta, Phys. Rev. 46 (1934) 1087.
[155] D.L. Burke, R.C. Field, G. Horton-Smith, J.E. Spencer, D. Walz, et al., Positron production in multiphoton light-by-light scattering, Phys. Rev. Lett. 79 (1997) 1626.
[156] A.R. Bell, J.G. Kirk, Possibility of prolific pair production with high-power lasers, Phys. Rev. Lett. 101 (2008) 200403.
[157] S.S. Bulanov, N.B. Narozhny, V.D. Mur, V.S. Popov, Electron-positron pair production by electromagnetic pulses, JETP 102 (2006) 9.
[158] M. Jirka, O. Klimo, S.V. Bulanov, T.Zh. Esirkepov, E. Gelfer, et al., Electron dynamics and γ and e^+e^- production by colliding laser pulses, Phys. Rev. E 93 (2016) 023207.
[159] T. Grismayer, M. Vranic, J.L. Martins, R.A. Fonseca, L.O. Silva, Laser absorption via quantum electrodynamics cascades in counter propagating laser pulses, Phys. Plasmas 23 (2016) 056706.
[160] E.G. Gelfer, A.A. Mironov, A.M. Fedotov, V.F. Bashmakov, I.Y. Kostyukov, et al., Perspectives of implementing QED cascade production with the next generation of laser facilities, J. Phys. Conf. Ser. 594 (2015) 012054.
[161] M. Vranic, T. Grismayer, R.A. Fonseca, L.O. Silva, Electron-positron cascades in multiple-laser optical traps, Plasma Phys. control. Fusion 59 (2016) 014040.
[162] E. Gelfer, H. Kadlecova, O. Klimo, S. Weber, G. Korn, Gravitational waves generated by laser accelerated relativistic ions, Phys. Plasmas 23 (2016) 093107.
[163] A. Faenov, J. Colgan, S. Hansen, A. Zhidkov, T. Pikuz, et al., Nonlinear increase of x-ray intensities from thin foils irradiated with a 200 tw femtosecond laser, Sci. Rep. 5 (2015) 13436.
[164] Y. Zou, R. Hutton, F. Currell, I. Martinson, S. Hagmann (Eds.), Handbook for Highly Charged Ion Spectroscopic Research, Taylor & Francis Inc, 20 September 2011. ISBN-10: 1420079042, ISBN-13: 978-1420079043.
[165] A. Faenov, I. Skobelev, T. Pikuz, S. Pikuz, R. Kodama, et al., Diagnostics of warm dense matter by high-resolution x-ray spectroscopy of hollow ions, Laser Part. Beams 33 (2015) 27.
[166] J. Colgan, J. Abdallah, A. Faenov, S. Pikuz, E. Wagenaars, et al., Exotic dense matter states pumped by relativistic laser plasma in the radiation dominant regime, Phys. Rev. Lett. 110 (2014) 125001.
[167] F. Rosmej, R. Dachicourt, B. Deschaud, D. Khaghani, M. Dozieres, et al., Exotic x-ray emission from dense plasmas, J. Phys. B At. Mol. Opt. Phys. 48 (2015) 224005.
[168] E. Galtier, A. Moinard, F. Khattak, O. Renner, T. Robert, et al., High resolution x-ray imaging of k-alpha radiation induced by high intensity laser pulse interaction with a copper target, J. Phys. B At. Mol. Opt. Phys. 45 (2012) 205701.
[169] F. Condamine, R. Lotzsch, I. Uschmann, O. Renner, O. Klimo, et al., Ultra-fast dynamics of charge state distribution driven by suprathermal electrons generated from laser solid matter interaction at relativistic laser intensities, (to be submitted).
[170] O. Renner, R. Liska, F. Rosmej, Laser-produced plasma-wall interaction, Laser Part. Beams 27 (2009) 725.
[171] E. Oks, Plasma Spectroscopy: The Influence of Microwave and Laser Fields, Springer Verlag, Berlin, 1995.
[172] M. Tatarakis, I. Watts, F. Beg, E. Clark, A. Dangor, et al., Laser technology: measuring huge magnetic fields, Nature (London) 415 (2002) 280.
[173] O. Renner, P. Sauvan, E. Dalimier, C. Riconda, F. Rosmej, et al., Signature of externally introduced laser fields in x-ray emission of multicharged ions, High. Energy Density Phys. 5 (2009) 139.
[174] S. Ferri, A. Calisti, C. Mosse, L. Mouret, B. Talin, et al., Frequency-fluctuation model applied to stark-zeeman spectral line shapes in plasmas, Phys. Rev. E 84 (2011) 026407.

[175] E. Stambulchik, Y. Maron, Zeeman effect induced by strong laser light, Phys. Rev. Lett. 113 (2014) 083002.
[176] R. Loetzsch, O. Jäckel, S. Höfer, T. Kämpfer, J. Polz, et al., K-shell spectroscopy of silicon ions as diagnostic for high electric fields, Rev. Sci. Instr. 83 (2012) 113507.
[177] G. Fiksel, W. Fox, A. Bhattacharjee, D.H. Barnak, P.-Y. Chang, et al., Magnetic reconnection between colliding magnetized laser-produced plasma plumes, Phys. Rev. Lett. 113 (2014) 105003.
[178] B. Albertazzi, A. Ciardi, M. Nakatsutsumi, T. Vinci, J. Beard, et al., Laboratory formation of a scaled protostellar jet by coaligned poloidal magnetic field, Science 346 (2014) 325.
[179] O.V. Gotchev, J.P. Knauer, P.Y. Chang, N.W. Jang, M.J. Shoup III, et al., Seeding magnetic fields for laser-driven flux compression in high-energy-density plasmas, Rev. Sci. Instrum. 80 (2009) 043504.
[180] P.Y. Chang, G. Fiksel, M. Hohenberger, J.P. Knauer, R. Betti, et al., Fusion yield enhancement in magnetized laser-driven implosions, Phys. Rev. Lett. 107 (2011) 035006.
[181] K.B. Fournier, J.D. Moody, Report on the B-fields at NIF workshop held at LLNL October 12−13, 2015, Tech. Rep. Lawrence Livermore Natl. Lab., 2016. URL:https://lasers.llnl.gov/content/assets/docs/for-users/report_on_the_b-field_workshop.pdf.
[182] G. Fiksel, A. Agliata, D. Barnak, G. Brent, P.-Y. Chang, et al., Note: experimental platform for magnetized high-energy-density plasma studies at the omega laser facility, Rev. Sci. Instrum. 86 (2015) 016105.
[183] B.B. Pollock, D.H. Froula, P.F. Davis, J.S. Ross, S. Fulkerson, et al., High magnetic field generation for laser-plasma experiments, Rev. Sci. Instrum. 77 (2006) 114703.
[184] S.P. Hatchett, C.G. Brown, T.E. Cowan, E.A. Henry, J.S. Johnson, et al., Electron, photon, and ion beams from the relativistic interaction of petawatt laser pulses with solid targets, Phys. Plasmas 7 (2000) 2076.
[185] P.A. Norreys, M. Santala, E. Clark, M. Zepf, I. Watts, et al., Observation of a highly directional γ-ray beam from ultrashort, ultraintense laser pulse interactions with solids, Phys. Plasmas 6 (1999) 2150.
[186] C.D. Chen, J.A. King, M.H. Key, K.U. Akli, F.N. Beg, et al., A bremsstrahlung spectrometer using k-edge and differential filters with image plate dosimeters,, Rev. Sci. Instrum. 79 (2008) 10E305.
[187] J.H. Jeon, K. Nakajima, H.T. Kim, Y.J. Rhee, V.B. Pathak, et al., A broadband gamma-ray spectrometry using novel unfolding algorithms for characterization of laser wakefield-generated betatron radiation, Rev. Sci. Instrum. 86 (2015) 123116.
[188] S. Sakata, Y. Arikawa, S. Kojima, T. Ikenouchi, T. Nagai, et al., Photonuclear reaction based high-energy x-ray spectrometer to cover from 2 MeV to 20 MeV, Rev. Sci. Instrum. 85 (2014) 11D629.
[189] M.A. Espy, A. Gehring, A. Belian, T. Haines, J. Hunter, et al., A wide-acceptance compton spectrometer for spectral characterization of a medical x-ray source, Proc. SPIE 9783 (2016) 97834V.
[190] S. Singh, A. L. Garcia, A. Ferrari, M. Molodtsova, L. Morejon, et al., Absolute calibration of a compact gamma-ray spectrometer for high intensity laser plasma experiments (In preparation).
[191] S. Kneip, C. McGuffey, J. Martins, C. Bellei, V. Chvykov, et al., Bright spatially coherent synchrotron X-rays from a table-top source, Nat. Phys. 6 (2010) 980.
[192] Z. Najmudin, S. Kneip, M.S. Bloom, S.P.D. Mangles, O. Chekhlov, et al., Compact laser accelerators for x-ray phase-contrast imaging, Philo. Trans. Royal Soc. London a: Mathematical, Physical and Engineering Sciences 372 (2014).
[193] F. Dorchies, V. Recoules, J. Bouchet, C. Fourment, P.M. Leguay, et al., Time evolution of electron structure in femtosecond heated warm dense molybdenum, Phys. Rev. B 92 (2015) 144201.
[194] A. Poyé, S. Hulin, M. Bailly-Grandvaux, J. Dubois, J. Ribolzi, et al., Physics of giant electromagnetic pulse generation in short-pulse laser experiments, Phys. Rev. E 91 (2015) 043106.
[195] A. Poyé, J. Dubois, F. Lubrano-Lavaderci, E. D'Humiéres, M. Bardon, et al., Dynamic model of target charging by short laser pulse interactions, Phys. Rev. E 92 (2015) 043107.
[196] J. Dubois, F. Lubrano-Lavaderci, D. Raffestin, J. Ribolzi, J. Gazave, . Tikhonchuk, et al., Target charging in short-pulse-laser-plasma experiments, Phys. Rev. E 89 (2014) 013102.
[197] C. Stoeckl, V. Glebov, P. Jaanimagi, J. Knauer, D. Meyerhofer, et al., Operation of target diagnostics in a petawatt laser environment (invited), Rev. Sci. Instrum. 77 (2006) 10F506.
[198] M. DeMarco, J. Krasa, J. Cikhardt, M. Pfeifer, E. Krousky, et al., Measurement of electromagnetic pulses generated during interactions of high power lasers with solid targets, J. Inst. 11 (2016) C06004.
[199] M. Mead, D. Neely, J. Gauoin, R. Heathcote, P. Patel, Electromagnetic pulse generation within a petawatt laser target chamber, Rev. Sci. Instrum. 75 (2004) 4225.
[200] Virtual Lab from Lighttrans: http://www.lighttrans.com.